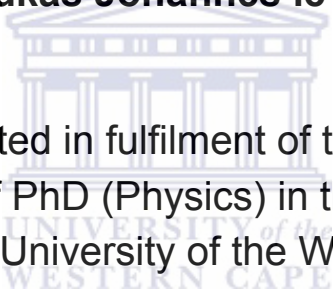# The Effects of Reverse Bias on
the Efficiency of Dye Solar Cells

Lukas Johannes le Roux

A thesis submitted in fulfilment of the requirements for
the degree of PhD (Physics) in the Department of
Physics, University of the Western Cape.

Promoter: Dr S Hietkamp (CSIR)
Co-promoter: Prof D Knoesen (UWC)

August 2009

ABSTRACT

Dye-sensitised solar cells (DSC) have attracted much attention during the last few years due to their high efficiencies and their potentially low production costs. The technology is based on a thin layer of nano sized, high band gap (3.2 eV) TiO_2 film. A Ru containing dye (from hereon called the Ru dye) is chemisorbed onto the TiO_2 film. This combination acts as the working electrode. The counter electrode consists of a platinum layer which is the catalyst for the regeneration of the Iodine/Iodide electrolyte.

The work that is presented here is focused on the results that were obtained during studies of the performance of the DSC under certain reverse bias conditions. When one cell in the series connection in a module is shaded, the current will pass this cell in reverse bias. In such a case the shaded cell will be subjected to a voltage in the reverse direction coming from the other lit cells in the module. This reverse voltage could permanently modify or damage the cell if it is not properly protected. Although the work is focussed on the chemical stability of the dye, various techniques were employed to determine the physical changes in the cell.

It was found that a cell that was subjected to a reverse bias of 2 V for 500 min showed a 58% recovery and a cell that was subjected to 4.5 V reverse bias was irreversibly damaged.

The UV-vis spectra showed a blue shift (higher energy), the Raman showed no peak at 1713 cm^{-1} (which indicates the absence of free carboxylate groups) and the FT-IR showed the disappearance of the N-C-S absorption band at 2100 cm^{-1}. The combined conclusion is that the –NCS ligand has been depleted and replaced with I_3^- ions.

When measuring the impedance, the Nyquist plots showed an increase in the charge transfer resistance at the counter electrode when subjected to

a reverse bias potential of 2 V. This is confirmed by the Bode plots. This indicates a partial oxidation of the Pt catalyst on the counter electrode. It can therefore be stated with confidence that the changes in the cell after being subjected to a reverse bias potential of 2 V for 500 min are changes on the -NCS bonds on the Ru dye as well as the Pt in the counter electrode.

UNIVERSITY *of the*

WESTERN CAPE

Declaration

I declare that "The Effects of Reverse Bias on the efficiency of Dye Solar Cells" is my own work, that it has not been submitted before for any degree or examination in any other university, and that all the sources I have used or quoted have been indicated and acknowledged as complete references.

Lukas Johannes le Roux   August 2009

Signed: . . . .

UNIVERSITY *of the*
WESTERN CAPE

ACKNOWLEDGEMENTS

CONTENTS

UNIVERSITY *of the*
WESTERN CAPE

LIST OF ABBREVIATIONS

ACN = acetonitrile

ASTM = American Society for Testing and Materials

ATR = attenuated total reflectance

CB = conduction band

CCD = charged coupled device

CL = cathodoluminiscence

CT = charge transfer

DSC = dye solar cell

E = electrode potential

E°' = standard electrode potential

EBIC = electron beam induced current

EBSD = electron back scattered diffraction

EDS = energy dispersive X-ray spectroscopy

EIS = electrochemical impedance spectroscopy

F = Faraday constant ($9.6485309*10^4$ C mol^{-1})

HOMO = highest occupied molecular orbital

i = $\sqrt{-1}$ (imaginary number)

I = current

ICDD = International Centre Diffraction Data

I_{sc} = short circuit current

ITO = Indium tin oxide

J = current density

J_{sc} = short circuit current density

LBIC = laser beam induced current

LUMO = lowest unoccupied molecular orbital

n = number of electrons transferred in the half reaction

NMMU = Nelson Mandela Metropolitan University

Ox = oxidation

PN = propionitrile

R = universal gas constant (8.314510 J K^{-1} mol^{-1})

RB = reverse bias

R_{ct} = charge transfer resistance

Red = reduction

Redox = reduction/oxidation

RR = resonance raman

SEM = scanning electron microscope

T = temperature in Kelvin

TBA = tetra butyl ammonium

TCO = transparent conductive oxide

UWC = University of the Western Cape

VB = valence band

V_{oc} = open circuit voltage

CHAPTER 1

1 INTRODUCTION

The history of dye-sensitisation dates back to the 19th century, when photography was invented. Hermann Wilhelm Vogel, a German photochemist and photographer (Leggat 1999) made key contributions to practical color photography. This work can be considered the first significant study of dye-sensitisation of semiconductors. He discovered how to increase the sensitivity of photographic emulsions, where silver halide emulsions were sensitised by dyes to produce black and white photographic films. Albert Einstein described the phenomenon of the photovoltaic effect in 1904 and was awarded the Nobel Prize for his explanation in 1921 (http://almaz.com/nobel/nobel.html, 2006).

The technique of dye-sensitisation in photovoltaics remained rather unsuccessful until a breakthrough at the early 1990's in the Laboratory of Photonics and Interfaces in the EPFL Switzerland. Professor Grätzel and his co-workers developed a solar cell with energy conversion efficiency exceeding 7% (O'Regan & Grätzel, 1991) and 10% in 1993 (Nazeeruddin *et al.*). This solar cell is called the dye sensitised nanostructured solar cell or the Grätzel cell after its inventor.

The dye-sensitised solar cell (DSC) is a photoelectrochemical solar cell i.e. it uses a liquid electrolyte or other ion-conducting phase as a charge transport medium. This is different to the all-solid conventional semiconductor solar cells that work on a p-n junction principle. The research interest in the DSC technology grew rapidly during the 1990's due to the higher efficiencies and good long-term stability that was reported. According to the work reported by Halme,

(2006), numerous research groups explored the replacement of the liquid electrolyte with solid or less volatile products.

The high cost of solar cells is one of the most significant factors that prevented the implementation of this technology on a large scale. Silicon solar cell technology is mature and the only reduction in cost is the economies of scale. There is therefore a need for the development of new materials and concepts for photovoltaic conversion to produce lower cost cells.

In real life situations, one or more cells in a module can be partially shaded, which results in electrical mismatching and the cell is subjected to reverse bias. The electrons then flow into the cell instead of out. This could irreversibly damage the cells if the voltage is large enough. To prevent damage to cells due to reverse bias, diodes are incorporated in the circuit to prevent any possibility of reverse bias. This research looks at the effects that reverse bias has on DSCs. Future work could lead to the possibility to design modules in such a way that no diodes would be necessary, thereby reducing the cost further.

2   BACKGROUND

2.1   Operating Principles of Crystalline Silicon Cells

The standard silicon solar cell is based on a semiconductor p-n junction. The cell consists of n-doped and p-doped semiconductor layers. When the two layers are placed in contact with each other the p-n junction (Markvart and Castañer, 2003) is formed by the charge carriers from n-type (electrons) and p-type (holes) layers respectively. Figures 2.1 and 2.2 depict the affect of doping on the mechanism.

N-type semiconductors are obtained by adding an impurity (doping) such as arsenic or phosphorus atoms having an excess valence electron in comparison with Si. The n-type doping results in energy states just below the conduction band of the host semiconductor.
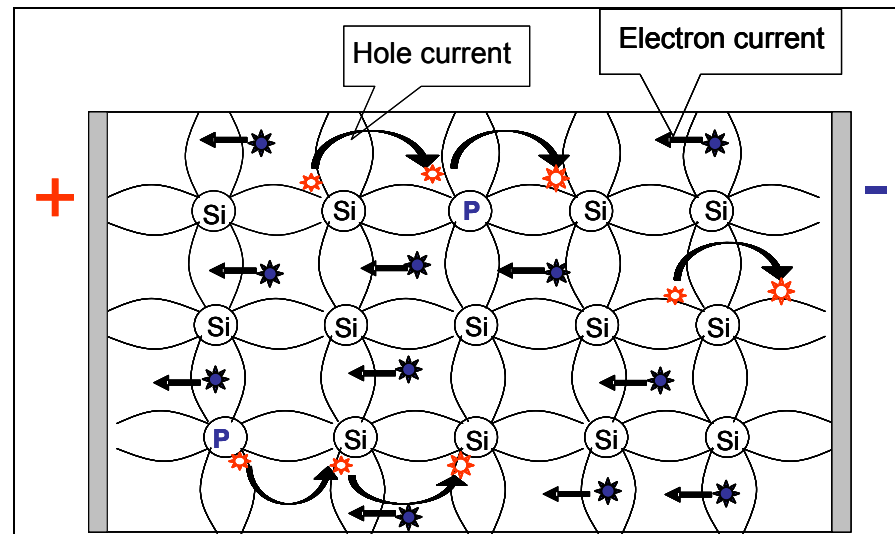
Figure 2.1: N-type semiconductor

P-type semiconductors are usually obtained by doping the silicon with boron (aluminium or gallium atoms can also be used) which has one valence electron less than the surrounding atoms. P-type doping results in empty states with energy slightly above the valence band of the semiconductor.
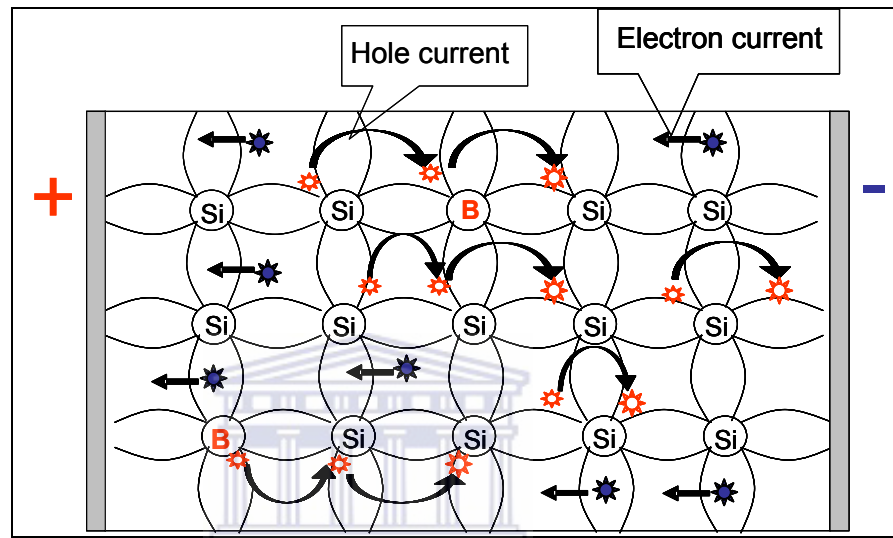
Figure 2.2: P-type semiconductors

When the n-type and p-type semiconductors are joined together a movement of electrons and holes across the junction takes place until equilibrium is reached. This is called the equalisation of the Fermi energy level in the materials which is explained in more detail in 2.1.1. This process sets up a depletion zone (see Figure 2.3.) near the junction where there are practically no free charges. An electric field (potential difference) exists across the region.
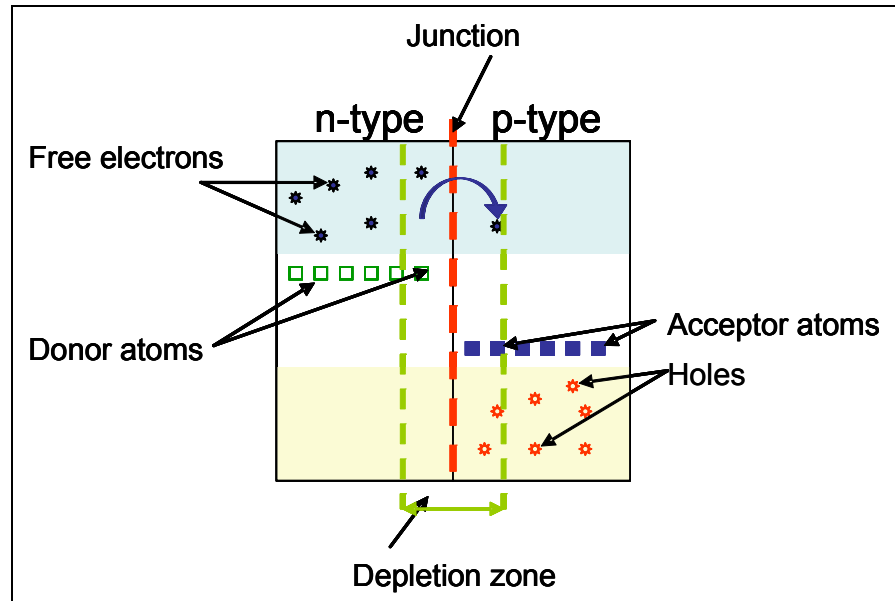
Figure 2.3: Schematic diagram of a crystalline Silicon cell

2.1.1 Charge equilibrium

When the electrons/holes close to the junction diffuse across the junction into the *p*-type/*n*-type region, the cell would reach charge equilibrium. This process leaves the ionised donors (acceptors) behind, creating a region around the junction, which is depleted of mobile carriers. This region is called the depletion zone and extends from $x = -x_p$ to $x = x_n$ (see Figure 2.4.) The charge due to the ionised donors and acceptors creates an electric field, which in turn causes a drift of carriers in the opposite direction. The diffusion of carriers continues until the drift current balances the diffusion current, thereby reaching charge equilibrium as indicated by a constant Fermi energy. This phenomenon is shown in Figure 2.4:
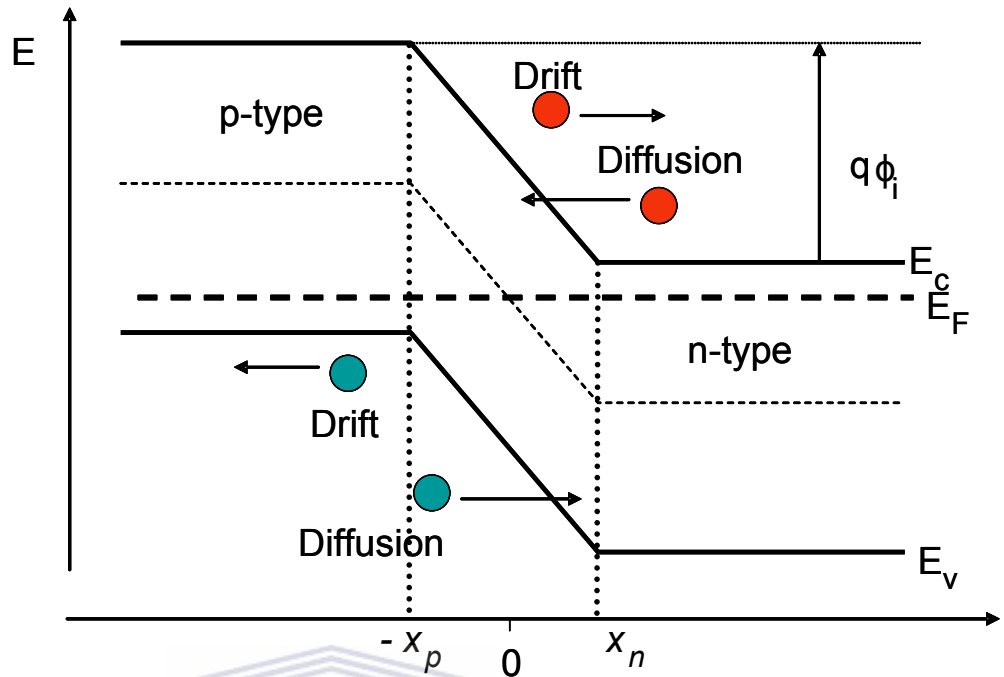
Figure 2.4: Energy band diagram of a p-n junction in charge equilibrium

E_c = energy at the conduction band

E_F = Fermi energy level

E_v = Energy at the valence band

There is an internal potential (built-in potential), $q\phi_i$, which is caused by the difference between the *n*-type and *p*-type semiconductors. This built-in potential in a semiconductor is the potential across the depletion region (between $-x_p$ and x_n in Figure 2.4). The following expression can be used to calculate the built-in potential (voltage). (Van Zeghbroeck, 2004)

$$\phi_i = V_f \ln \frac{N_d \, N_a}{n^2_i} \qquad \textit{equation 2.1}$$

Where:

N_a = Acceptor density in the *p*-type region per cm^3

N_d = Amount of donors in the *n*-type region per cm^3

n^2_i = amount of positive (or negative) charge carriers per cm^3

$V_f = k_b T/q$ (volts)

k_b = Bolzmann's constant 1.38 x 10^{-23} JK^{-1}

$k_b T$ = kinetic energy in eV

q = charge of an electron 1.602x10^{-19} C

2.1.2 The basic steps of photovoltaic energy conversion

Three basic steps needed for a photovoltaic cell to work are:

1. Light absorption
2. Charge separation
3. Charge collection

The physical or chemical processes behind these principal steps vary between different types of solar cells and photovoltaic materials. The efficiency of a solar cell depends on the efficiency of each of these steps and is maximised by the materials selection including the cell design (Bach, *et al*., 1999).

2.1.3 The functioning of a Si-based photovoltaic cell

The illumination of the p-n junction causes excitation of electrons from the valence band (VB) to the conduction band (CB) leaving holes in the valence band. The electrons and holes are almost free to move in the material due to the Fermi energy and also by diffusion due to concentration differences.

During illumination, depending on the light intensity, a large number of electrons are excited to the conduction band and holes are generated in the semiconductor material. Electrons are accumulated in the n-type material and holes in the p-type material which causes a potential difference (voltage) between

the opposite sides of the p-n junction. Electrical contacts can be attached to an external load which will complete the circuit.

2.2 Operating Principles of the DSC

The working mechanism and components of a DSC

The DSC comprises:

1. A transparent conducting glass electrode (Indium tin oxide – ITO) coated with porous nanocrystalline TiO_2.

2. Dye molecules are chemically adsorbed to the surface of the TiO_2. Figure 2.5 shows a diagram of the cell configuration.

3. A reduction-oxidation (redox) electrolyte couple (I^-/I_3^-) and a counter-electrode coated with a Pt catalyst on an ITO layer, makes up the rest of the configuration. During illumination the cell produces a voltage over and current through, an external load that is connected to the electrodes.

The absorption of light in the DSC occurs in the dye molecules. The charge separation by electron injection (Bauer, *et al*., 2002) from the dye to the TiO_2 occurs at the TiO_2/electrolyte interface (Figure 2.5). Figure 2.5 shows schematically the relative energy levels of the dye in a working DSC as well as the regenerative working cycle of the cell.
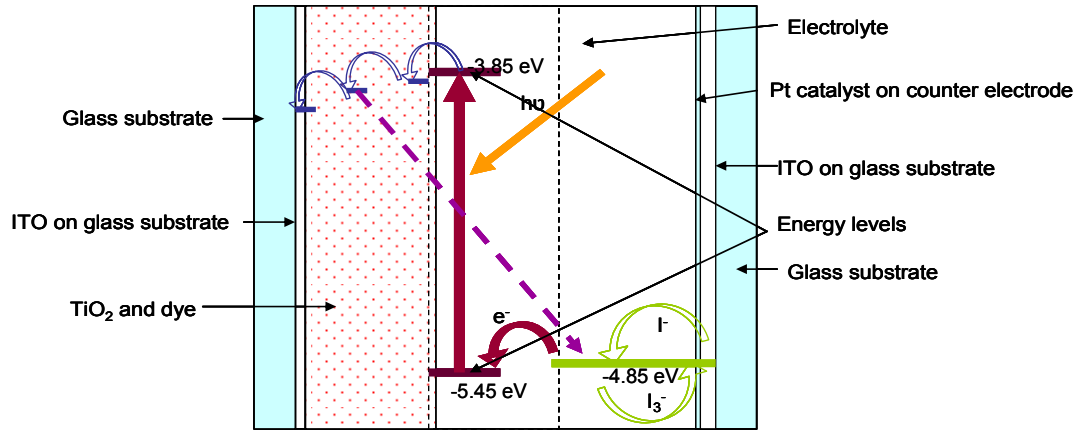
Figure 2.5: Diagram of the cell configuration. (Values were obtained from Lenzmann *et al.,* (2001).

The TiO$_2$ as an electrode is ideal for the optical operation because of it's large band gap and absorbance at wavelengths below 400 nm (Figure 2.6). The major part of the solar spectrum is therefore available for absorption by the dye molecules.
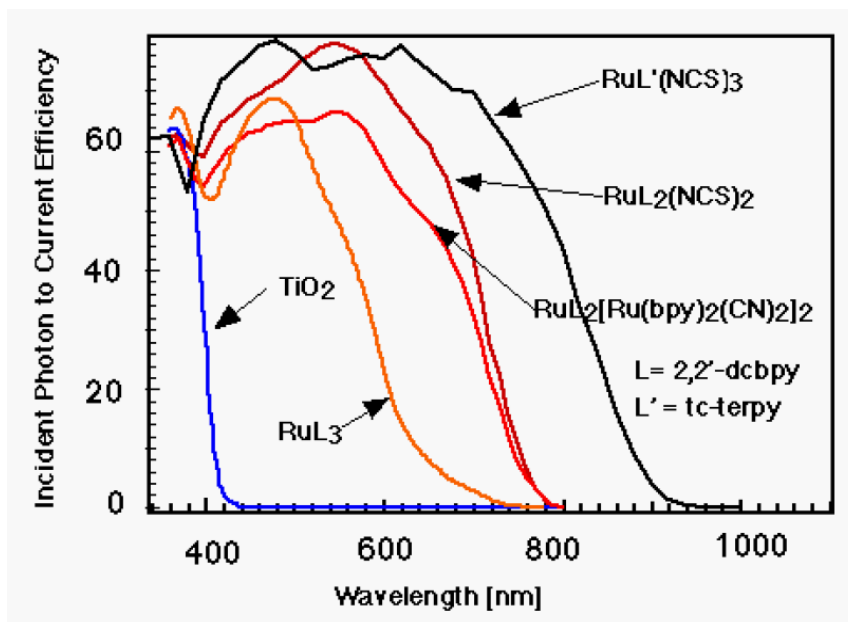
Figure 2.6: Absorption spectrum of TiO_2 and some of the Ru-dyes that are used in the DSC research (Grätzel & McEvoy 2004)

2.2.1 Open-Circuit Voltage

During photo excitation of the dye molecules, which is typically an organometallic Ru compound, (Figure 2.5) electrons are injected into the conduction band of the TiO_2 layer. The absorption starts roughly at 720 nm for most dyes. The electrons travel through the semiconductor, exit at the working electrode contact, flow through an applied external load, and then react with the adsorbed oxidised half (catalysed by Pt layer) of the redox couple at the counter electrode/electrolyte interface.

The injected electrons can however, undergo unwanted surface recombination with either the oxidised half of the redox couple in solution or with the oxidised dye molecules. According to Hagfeldt and Grätzel (1995), the high concentration of I^- ions that are present in the cells, results in the fact that

12

recombination of injected electrons with the dye molecules can be neglected.

Figure 2.7 shows the chemical reactions as they occur in a typical DSC. The incoming photon is absorbed by the dye molecule which is adsorbed on the surface of the nanocrystalline TiO_2 particle and an electron from a molecular ground state Ru(II) is excited to a higher lying excited state Ru(II)* (photo excitation).

The excited electron is injected into the conduction band of the TiO_2 particle resulting in changing the Ru in the dye molecule in an oxidised state [Ru(III)] (electron injection). The injected electrons flow through the porous TiO_2 structure to the conducting oxide layer of the glass substrate (anode) and finally through an external load back to the counter-electrode (cathode). At the counter-electrode the electron is transferred to the triiodide in the electrolyte to yield iodide, and the cycle is closed by reduction of the oxidised dye by the iodide in the electrolyte which is then converted back to the triiodide (I_3^-). Recombination involving triiodide can occur at the semiconductor/electrolyte interface and then only if the electron can get in reach of the triiodide (Haque *et al.,* 1998 and 2000).

A potential difference between the electrodes results due to the energy levels in the system (Figure 2.5). The Pt on the counter electrode acts as a catalyst for the regeneration of the electrolyte. Cahen *et al.,* (2000) states that the maximum theoretical value for the photo voltage at open circuit condition is determined by the potential difference between the conduction band of the TiO_2 and the redox potential of the I^-/I_3^-.

The operation of the cell is regenerative in nature, i.e. chemical substances are neither consumed or produced during the working cycle. Theoretically the DSC should therefore be able to last forever.

$$Ru(I) \xrightarrow{h\upsilon} Ru(I)^* \quad \text{Photo excitation of the Ruthenium complex}$$

$$TiO_2 + Ru(I)^* \longrightarrow TiO_2(e) \quad Ru(II) \quad \text{electron injection}$$

$$3 - \xrightarrow{2Ru(III} 2Ru(II) \quad ^-_3 \quad \text{regeneration of} Ru(I) \text{ by iodide at } TiO_2 \text{ fil}$$

$$I^-_3 + \quad - \longrightarrow 3 - \quad \text{regeneration of iodide from triiodide at Pt electrode}$$
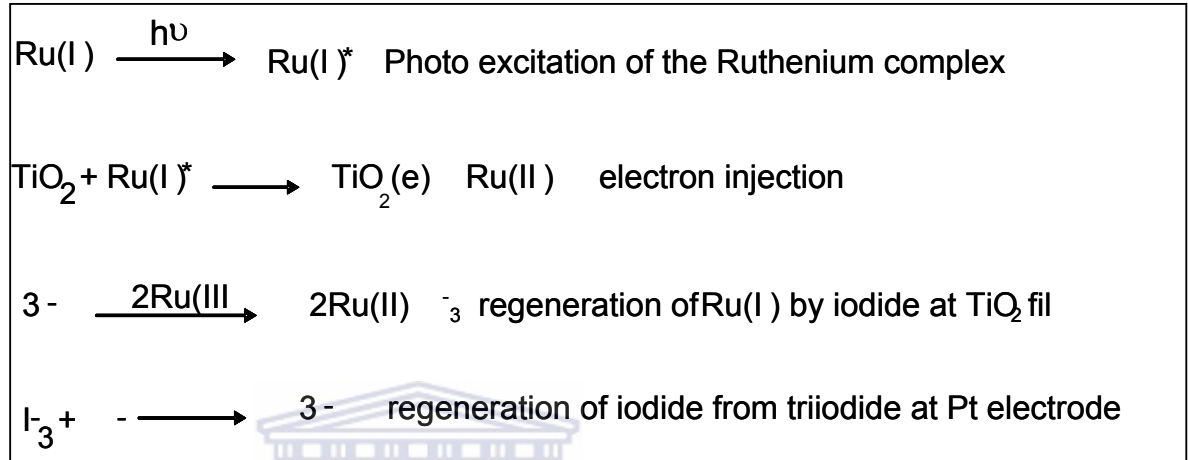
Figure 2.7: Chemical reaction cycle in the DSC.

2.2.2 Light Absorption

Why nano?

One of the challenges during the early development of the DSC was the low absorption capacity of the dye. The small quantity of dye on the TiO_2 caused that the incident light that could be absorbed by the dye was less than one percent. If more dye layers were deposited on the TiO_2, not all the dye would be in contact with the TiO_2, which would still result in low conversion efficiency. A nanoporous layer of TiO_2 with a surface area of about 300 m^2/g (previously 10 m^2/g) was developed to overcome this problem (O'Regan & Grätzel 1991).

The efficiency of the dye-sensitised solar cell depends on a collective effect of numerous physical and chemical nanoscale properties. The key issue however, is the principle of dye-sensitisation of large band-gap semiconductor electrodes. This

is accomplished by coating the internal TiO_2 electrode with dye molecules that can absorb the incoming photons. The molecular structures of three efficient photo sensitisers for DSCs that includes the "N3" dye and the "black" dye are presented in Figure 2.8.

The black dye, also known as Ru 620 or N-749 (Hedbor, 2005) and the N3 dye are considered the most efficient sensitisers for the conversion of light to electricity with TiO_2 as the semiconductor (Bauer *et al.,* 2002).

Work that was done by Kuang *et al.,* (2006) showed that the transition responsible for the broad absorption band around 750 nm is a ligand to-metal charge-transfer (LMCT) transition. The black dye absorbs light up to 900 nm (100 nm more than the N3 dye), which results in a better overlap with the solar spectrum (see Figure 2.6).

Black dye

N719

N3
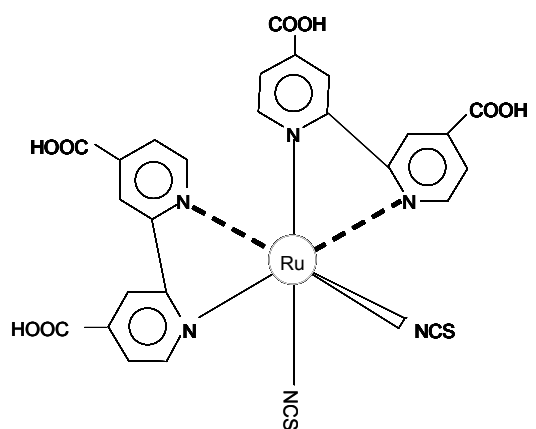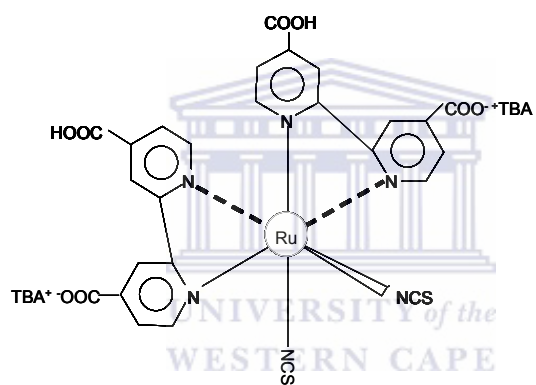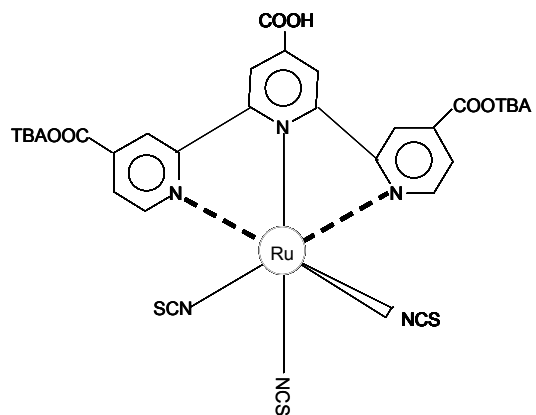
Figure 2.8: Molecular structures of three efficient dyes.

Johanssen (2006) investigated the effects of protonation on the efficiencies of the N719 and N3 dyes. By substituting some of the protons with tetrabutylammonium (TBA^+) higher open-circuit voltages resulted as well as lower short circuit currents and higher fill factors, which result in turn, in higher efficiency of the cells.

- Kalyanasundaram and Grätzel (1994) found that the trinuclear complex of Ru that has various bipyridyl units linked through the cyanide bridge is one of the most efficient sensitisers (Figure 2.9).
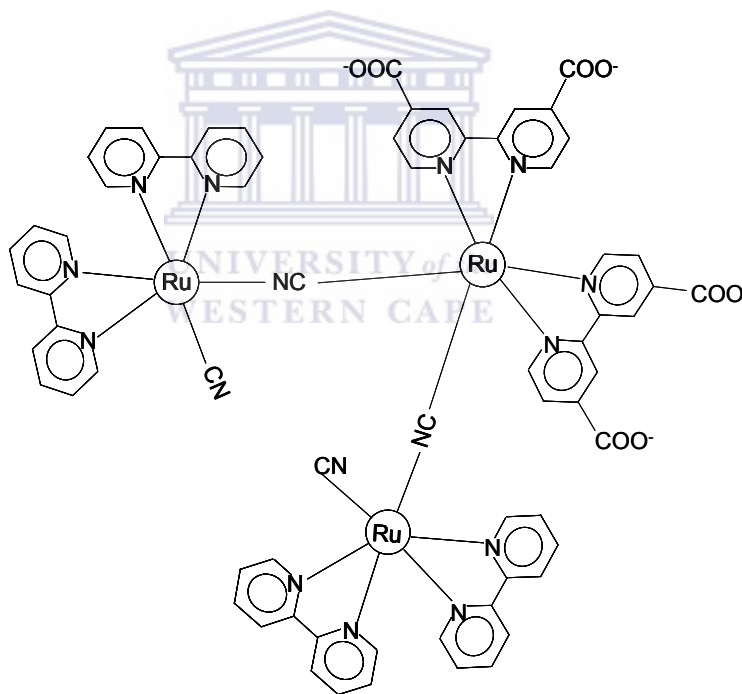
Figure 2.9: Cyano bridged trinuclear Ru complex [(CN)(bpy)$_2$-Ru-CN-Ru(dcbpy)$_2$-NC-Ru(bpy)$_2$(CN)].

The key chromophore carries carboxylic groups and can enhance the sensitisation capacity of a dye up to 10 times.

According to Kalyanasundaram and Grätzel (1994) some sort of surface chelation or derivatisation takes place with the carboxylic group as shown in Figure 2.10. Surface chelation is indicated by red-shift in the photocurrent. The spectra-maximum is usually observed at 515 nm but it shifted to 493 nm in solution (Kalyanasundaram and Grätzel, 1998).

The possible overlap of the π-orbitals of the 4,4'-dcpby with the 3d orbitals of the Ti(IV) will enhance the electronic coupling (Hagfeldt and Grätzel 1995). The surface chelation of the dyes is reversible and the dye can be bleached by stirring in alkaline solutions. This characteristic can be used to regenerate or recondition used cells and modules.
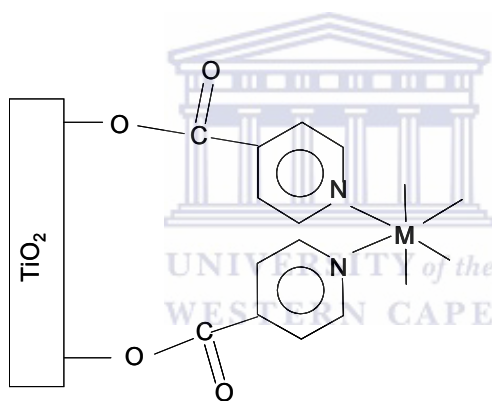
Figure 2.10: Carboxylic group coupling with the TiO$_2$

Finnie *et al.,* (1998) determined that the most likely configuration (supported by IR analysis) involves the attachment of the dye via two of the four carboxylate groups. They are either bridged between two adjacent rows of titanium ions through bidentate coordination or interact with surface hydroxyl groups through hydrogen bonds. In the N3 dye the two remaining carboxylate groups, one is ionised while the other remains in the protonated form. In the N719 dye, the two remaining carboxylate groups are reacted with tetrabutyl ammonium (TBA). There is no more free carboxylate groups in

the molecule, which resulted in the disappearing of the vibrational peak at 1715 cm^{-1}.

2.2.3 Recombination

Haque *et al.,* (1998) emphasised that the possibility of direct recombination between oxidised dyes and TiO_2 electrons may be an important process that limits the performance of photoelectrochemical cells. They determined that the kinetics of charge recombination between the oxidised dye and electrons within the TiO_2 were faster than re-reduction of the oxidised dye by I^-. This would suggest that for cell output voltages >0.6 V, direct recombination between the oxidised dye and electrons in the TiO_2 would result in a significant loss of photocurrent. (The redox potential of the I^-/I_3^- couple is approximately +0.2 V; therefore, a cell output voltage of 0.6 V corresponds to a Fermi level of the TiO_2 electrode of -0.4 V.) Recent models of the electrical performance of photoelectrochemical solar cells assumed that the recombination pathway is negligible and attributed the loss of current at high output voltages solely to recombination between the I_3^- ions and TiO_2 electrons (Haque *et al.,* 1998).

The charge recombination at the nanocrystallite-redox electrolyte interface is expected to play a significant role in lowering the photovoltage (Huang *et al.,* 1997). There are two likely recombination pathways occurring at the interface. The injected conduction-band electrons may recombine with oxidised dye molecules or react with the redox species in the electrolyte. The contribution of the energy-loss to the recombination current can usually be ignored due to the rapid rate of reduction of the dye molecules by the I^- ions, which are present at high concentration (Hagfeldt *et al.,* 1994). Kern *et al*.,

(2002) and Wang *et al.,* (2005) confirmed that the iodide does not contribute to the diffusion impedance due to the large excess of iodide relative to tri-iodide, and the diffusion constants of iodide and tri-iodide being of the same magnitude.

2.2.4 Electron migration and lifetime

The recombination of TiO_2 conduction band electrons with the holes in the electrolyte, i.e. I_3^-, is the most significant loss mechanism in the DSC. The electron transport by diffusion in the TiO_2 and their recombination with the electrolyte are the two competing processes in the DSC (Peter *et al.,* 2002). Figure 2.11 shows the reaction paths at the TiO_2 interfaces.
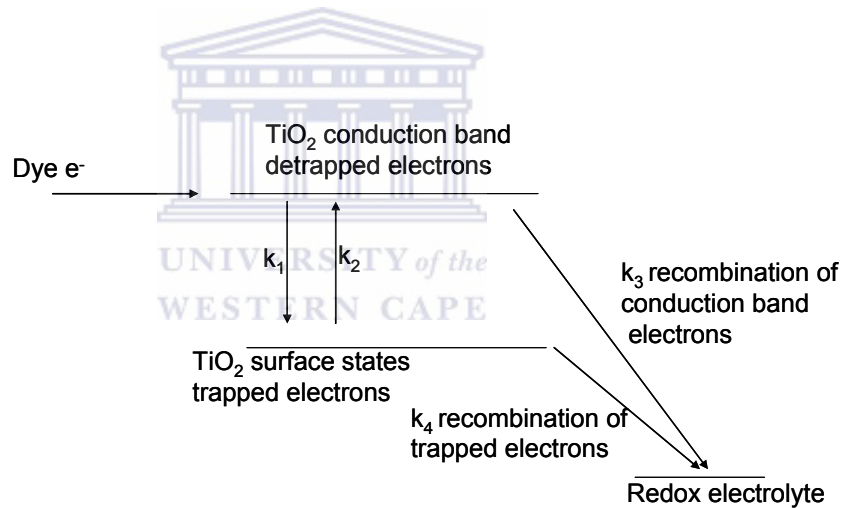
Figure 2.11: Reaction paths within a DSC at the TiO_2 interfaces where the following k values are attributed:

k_1, for the trapping of the conduction band electrons (about 1000 times faster than k_2)(Fischer *et al*., 2000);

k_2, for the detrapping of the electrons;

k_3, for the recombination of conduction band electrons;

k_4, for the recombination of trapped electrons.

Intensity modulated photovoltage spectroscopy (IMVS) measurements showed that the rate of reverse reaction of

photoinjected electrons with I_3^- is second order in total electron concentration (Fischer *et al.,* 2000 and Dloczik, *et al.*, 1997). This is in agreement with possible back reaction mechanisms of the electrons in the TiO_2 layer with the tri-iodide (Huang *et al.*, 1997). They used the second order back reaction both for the conduction band electrons as well as for the trapped electrons. Trapped electrons are on a layer just below the conduction band of the TiO_2 and they are not available for reaction or transfer. Fischer *et al.,* (2000) showed that trapping is about 1000 times faster than detrapping, so nearly all photoinjected electrons are located in trap or surface states rather than in the conduction band. Thus, the recombination of conduction band electrons with the electrolyte (k_3 n^2) can be neglected in comparison to the recombination of trapped electrons (k_4 N^2), *n* and *N* being the excess electron densities in the conduction band and the trap states, respectively. A recombination of electrons in the TiO_2 with the oxidised dye under open-circuit conditions Haque *et al.,* (1998) is also negligible.

This recombination model allows for the definition of effective transport parameters (Kern *et al.,* 2002). The effective lifetime of the electrons and the diffusion constant are:

$$\tau_{eff} = \frac{1}{2N_0 k_4} \qquad\qquad D_{eff} = D\, \frac{k_2}{k_1} \qquad\text{\textit{equation 2.2}}$$

where:

N_0 is the steady-state electron density in trap states.

D_{eff} is the effective electron diffusion constant in conduction band of the TiO_2 ($m^2\,s^{-1}$).

D is the electron diffusion constant in the bulk TiO_2 ($m^2\,s^{-1}$).

τ_{eff} is the effective lifetime of the electrons.

The rate constants for charge injection and iodide reduction are at least 109 times higher (Kohle *et al.,* 1997) than the rate constants for excited and oxidised state degradation. The sensitiser should be able to undergo around one billion cycles without significant degradation to be acceptable as a dye for the lifetime of a cell. Solaronix has performed various studies concerning the stability of the dye, the electrolyte, the redox couple, and the sealing of solar cells. The Ru(*dcbpy*)$_2$(NCS)$_2$ dye (also known as the N3 dye), has been validated for a commercial application. Light soaking experiments on photovoltaic devices at different temperatures have proved the long-term stability of this dye. The liquid electrolyte can be encapsulated for many years under thermal cycling with the suitable sealing material chemically inert to triiodide.
 (http://www.solaronix.com/technology/dyesolarcells/)(2005)

The rate constant for electron injection from the excited state to the conduction band of the TiO$_2$ particles is in the femtosecond range (100 fs). According to Grätzel (2006) the N3 dye can undergo photo-induced loss or exchange of the thiocyanate ligand, which occurs at a rate, much lower than 105 s^{-1}. It is not sure whether this pathway is destructive as the products that form, often iodo or solvato complexes, still act as charge transfer sensitisers.

The electron migration in the TiO$_2$ electrode as well as the electron back reaction with the redox electrolyte is strongly influenced by trapping and detrapping effects (Fischer *et al.,* 2000 and Peter *et al.,* 1999). This is also indicated by the very low values of the diffusion coefficient ($<10^{-4}$ cm^2 s^{-1}). Fischer *et al.,* (2000) describes the electron migration and back reaction in

terms of the electron diffusion length $L_n = (D_n \tau_n)^{1/2}$, where D_n is the electron diffusion coefficient and τ_n is the electron lifetime.

According to Bay and West (2005), the main factors limiting electron transport are interparticle electron hopping and intra-particle ohmic resistance.

2.3 Reverse bias

Reverse bias conditions occur when the voltage across a cell opposes the open circuit potential. A multi cell module might have one or more of its cells shaded out while operating in the open. When one cell in the series connection is shaded, the current will pass this cell in reverse bias. An example of such a case can be seen in Figure 2.12. In such a case the shaded cell will be subjected to a voltage in the reverse direction coming from the other lit cells in the module. The reverse voltage could adversely modify or damage the cell if it is not properly protected.
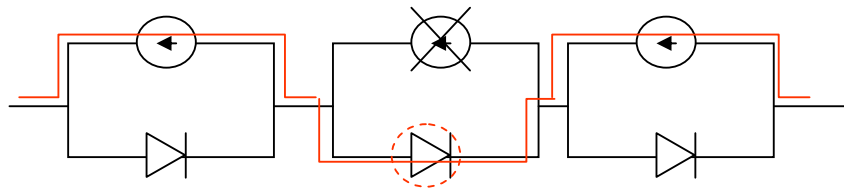
Figure 2.12: Example of the circuit where one cell is shaded

When a negative voltage is applied, the potential across the semiconductor increases as well as the depletion layer width. When a positive voltage is applied, the potential across the semiconductor and the depletion layer width will decrease. The total potential across the semiconductor equals the built-in potential minus the applied voltage (Figure 2.13).

Reverse bias   E   Forward bias

$E_{F,p}$

$q(\Phi_i - V_a)$

qV_a

E_c

$E_{F,n}$

$E_{F,p}$ qV_a

E_c

$E_{F,n}$

$q(\Phi_i - V_a)$

E_v

E_v

x
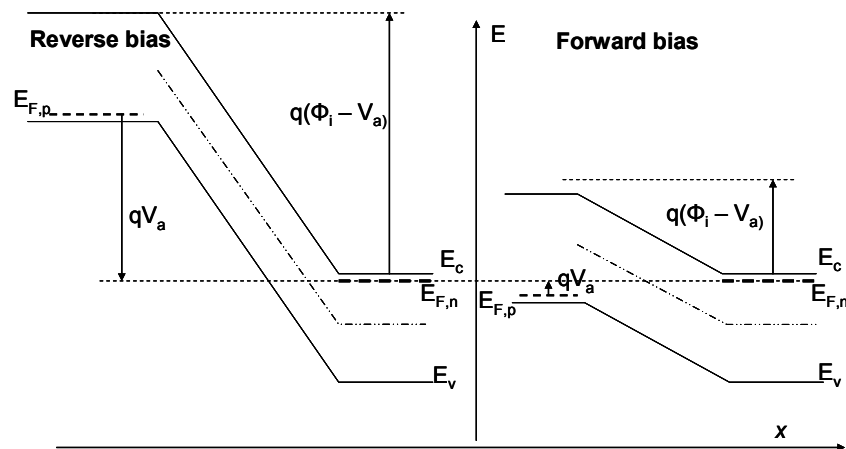
Figure 2.13: Schematic energy diagram of the change in energy levels when a cell is subjected to reverse and forward bias

E_c = energy at the conduction band

E_F = Fermi energy level

E_v = Energy at the valence band

N_a = Acceptor density in the *p*-type region per cm^3

N_d = Amount of donors in the *n*-type region per cm^3

n^2_i = amount of positive (or negative) charge carriers per cm^3

$V_f = k_b T/q$ (volts)

k_b = Bolzmann's constant 1.38 x 10^{-23} JK^{-1}

$k_b T$ = kinetic energy in eV

q = charge of an electron 1.602x10^{-19} C

According to Kern *et al.,* (2001) reverse biasing a DSC is not critical for stability thus integrated modules are possible without protection diodes on each cell.

When cells in a module are connected in series, the total voltage is the sum of the voltages of each individual cell. Sastrawan *et al.,* (2006) reported that when one cell in a module is completely shaded, the open-circuit voltage is reduced by the open-circuit voltage of the particular cell, plus

the voltage required to operate the shaded cell in reverse bias (about 300 mV). The applied voltage is proportional to the difference between the Fermi energy levels in the p-and n-type on both sides of the junction. Figure 2.14 gives an example of the break down voltage. The short-circuit current is only reduced very slightly, because of the low breakdown voltage of the DSCs.
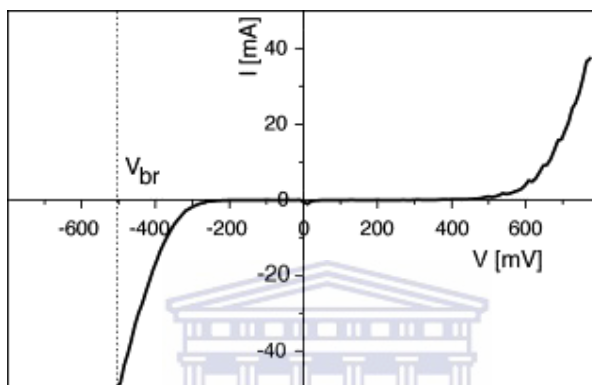
Figure 2.14: Measured *I–V* curve of a typical DSC (area = 2.5 cm^2) in the dark. The breakdown voltage (V_{br}) is at −500 mV. (Sastrawan *et al.,* 2006).

A reduction in the recombination rate is indicated by a positive shift in the breakdown voltage for the solar cells (Menzies *et al.,* 2007).

Methods of characterisation

DSC masterplates were prepared and were used as standard reference cells as the baseline for the research. The commercially available N719 dye was used in all cases except if stated differently.

The following techniques were used for the characterisation of cells:
• Potentiometry

Impedance spectroscopy gives information of the charge transfer and ionic transport while cyclic voltammetry can show changes in the cell due to oxidation or reduction of chemical species in a cell.

- Mobile Testing Station for Photovoltaics (MTSP)

The MTSP is a mobile test system especially for 3rd generation solar cells and modules, including the necessary hardware, software and portable computer. This equipment generates IV curves, fill factors, I_{sc}, V_{oc}, and cell efficiencies.

- UV/Visible

Absorption/transmission data for band gap determination and isosbestic points are used as reference points to determine reaction rates. A shift in the absorption maxima gives information of changes in the dye molecule.

The lowest energy peak was dominated by the nitrogen $2p$-orbital contributions to the π-electron system, whereas the second peak was made up mostly of the ring carbon $2p$-orbitals. The atomic orbitals centred on the -NCS ligands contributed to the highest energy valence orbital depopulated by the photon absorption. This orbital plays a key role in accepting an electron from the mediator in a Grätzel cell. The -NCS ligands are directed away from the semiconductor and toward the solution, therefore this type of dye should be particularly well suited to reduction from the electrolyte.

- IR and Raman spectroscopy

Chemical changes in the cell may be detected. So far it is not clear exactly what the actual changes are. The changes could be due to TiO_2, or TiO_2 and dye, or TiO_2 and dye and electrolyte. It can be determined whether the bonds between the carboxylate groups and the TiO_2 are still intact. Evidence of peaks at 1354 cm^{-1} and 1751cm^{-1}

are an indication of isolated (non bonded) carbonyl groups (Falaras *et al*., 1993). The vibrational band at ~2100 cm^{-1} is characteristic for the -NCS group and a change in the relative size of this peak would be indicative of either broken bonds or depletion of the -NCS group.

In the Raman spectra, the peaks assigned to C–C or C–N ring stretches, published by Falaras (1998), are observed at 1610, 1540, and 1470 cm^{-1} in samples.

- SEM, AFM

High-resolution surface morphology investigation and particle characterisation before and after the reverse bias experiments.

CHAPTER 3

3   OBJECTIVES OF THE RESEARCH

Reverse bias conditions occur when the voltage across a cell
opposes the open circuit potential (Wheatley *et al.,* 2003).

It has been reported that reverse bias has little on no effect
(Sastrawan *et al.*, 2006) on the stability of the dyes in the dye-
sensitised solar cells (DSCs). Wheatley *et al.,* (2003) however,
reported that when a DSC is subjected to a reverse bias of 2000 mV,
an irreversible loss of intensity in the metal to ligand charge transfer
band at 540 nm occurred.

The research goals were:
1. The determination the chemical change in the structure of the dye
   molecule after the application of reverse bias.
2. The determination of the effect of time and voltage on the rate
   and severity of the decomposition of the dye.
3. Analyses of the different interfaces in the cell were done to
   determine the reason(s) for lower efficiencies after certain reverse
   bias potentials.

CHAPTER 4

4 EXPERIMENTAL

4.1 Preparation of materials and components for DSC

4.1.1 Synthesis of nano TiO$_2$ sol from titanium n-butoxide.

Chemical reaction of the process

$$Ti\,(O\text{-}nBu)_4 + 2\,H_2O \quad \rightarrow \quad TiO_2 + 4\,n\text{-}BuOH$$
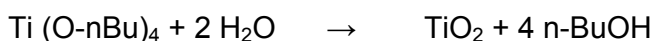
4.1.1.1 Materials and Reagents

Titanium (IV) n-butoxide Ti (C$_4$H$_9$O)$_4$, [Alfa products],
10% (v/v) nitric acid [Merck]

4.1.1.2 Method

The apparatus were set up as shown in Figure 4.1.

The 10% (v/v) Nitric acid was diluted to ~0.1M solution.

120 mℓ of titanium n-butoxide Ti(C$_4$H$_9$O)$_4$ was measured and carefully transferred into a dropping funnel.

Approximately 600 mℓ of the diluted Nitric acid was transferred into the reaction vessel.

Ti (C$_4$H$_9$O)$_4$ was slowly added drop wise into the nitric acid at room temperature.

The mixture was stirred vigorously with an overhead stirrer during the addition of the titanium n-butoxide.

A white precipitate of amorphous TiO$_2$ and a layer of n-butanol were formed under these conditions.

After the addition was completed, the mixture was stirred vigorously for 5 hours (rest of the day) at 80 °C.

A rotary evaporator was used to remove the solvents from the sol-gel.

Water was added to the sol-gel and the removal of the solvent was repeated to ensure that all the butanol was

removed azeotropically under reduced pressure. (The boiling point of the n-butanol/water azeotrope is 93 °C at atmospheric conditions and 29 °C at 30 mm Hg.)

Figure 4.1: The experimental set up for the sol-gel preparation

4.1.2 Preparation of nano-TiO$_2$ paste (water based)

4.1.2.1 Method

Variations of a standard formulation were made and tested on glass substrates to find a stable formulation of which the cured (at 450 °C) product did not crack.

Different concentrations of Degussa P25 nano TiO$_2$ particles were added to the CSIR nano TiO$_2$ to determine the optimum mixture that does not crack after curing.

The final formulation consisted of:

CSIR nano TiO$_2$ particles (11.8%)

Degussa P25 nano TiO$_2$ particles (3.0%)

Distilled water (73.4%)

HPMC (hydroxyl propyl methyl cellulose - Merck) (7.4%)

PEG 20 000 (polyethylene glycol - Merck) (4.4%)

The mass percentages in brackets are the amounts that were used in the final formulation.

If the fresh product was used for the thin film, no cracks appeared after or during the drying and curing processes. If it was used after a few days it produced films that cracked after treatment at 450 °C.

4.2 Single cell construction

4.2.1 Electrode preparation

The following diagram shows the different steps to assemble a DSC. Glass substrates should be cleaned with alcohol prior to assembly. Due to the possibility of contamination care must be taken not to touch the conductive side of the glass with bare hands.
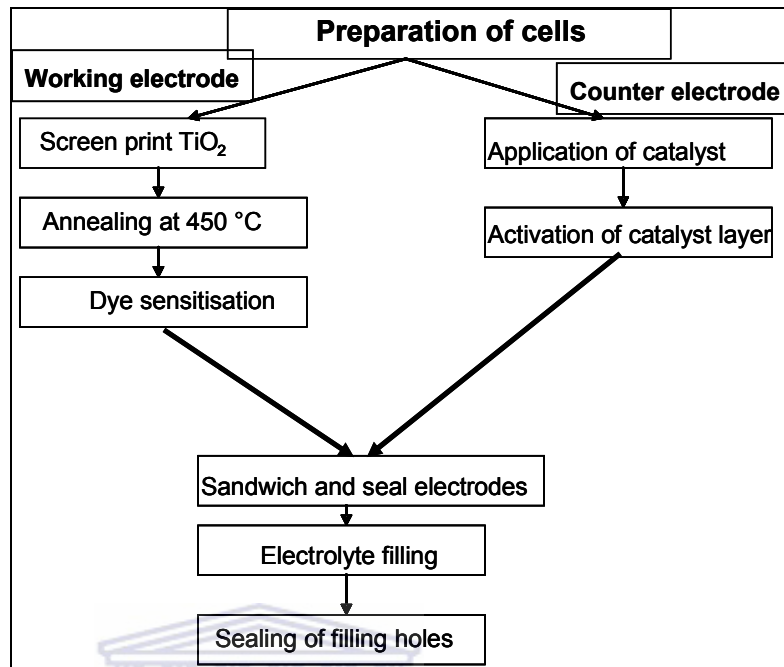
Figure 4.2: Diagram for the assembly of a DSC.

- After screen-printing the TiO_2 paste (working electrode) and catalyst (counter electrode), the glass substrates were cured in a furnace for 30 min at 450 °C.

- After curing and cooling, holes were drilled into the counter electrodes for the filling with the electrolyte.

  The following formulation was used as the electrolyte and was supplied by Solaronix.

  - 0.6M HMMI (hexylmethylimidazolium iodide)
  - 0.5M TBP (tertiary butyl pyridine)
  - 0.05M I_2 (iodine)
  - 0.1M LiI (lithium iodide)
  - Solvent: Acetonitrile (ACN)

- The two glass substrates were sealed together after which the electrolyte was introduced.

- The holes for the electrolytes were sealed.

4.2.2 Sealing of cells

4.2.2.1 ThreeBond 31X-100

This glue was obtained from ThreeBond in Japan. The cells were sealed by inserting the glue between the two glass electrodes and subjecting it to a wide spectrum UV source (10 nm to 400 nm).

After introduction of the electrolyte, the holes were sealed by sticking a piece of flat glass over the hole with the same glue.

When the cells were subjected to the UV source again after the electrolyte was added, the glue failed.

4.2.2.2 ThreeBond 31X-101

This glue was applied in the same manner as the 31X-100 and the performance was similar.

4.2.2.3 Polymer films

Two types of polymer sealants were tested; Surlyn 1702 and Amosil 4, both polymers from Du Pont and donated by ECN.

Surlyn 1702 is a low melting polymer (80 to 105 °C) and works well if the glass top is heated with a soldering iron. It softens at 75 °C and is therefore not the long-term answer for sealing.

Amosil 4 is a resin type sealant and is mixed with a hardener where after it is cured at room temperature.

4.2.3 Dye application

The dye (N719) is applied by dissolving 0.1 g in 50 mℓ dry ethanol (Merck). The working electrode is inserted in the

solution, covered with a watch glass and left overnight at room temperature or two hours at 40 °C.

The electrode is washed with dry ethanol and dried in an oven at 105 °C for 20 min.

4.2.4 Filling of cells

Depending on the size of the cell to be filled, either one or two holes are drilled in the counter electrode prior to sealing. The counter electrodes are submerged in water prior to drilling. The holes are drilled with a high-speed (8000 to 32000 rpm) drill and 1 mm tungsten carbide drill bits.

4.2.5 Master plate assembly as done at ECN (The Netherlands)

Master plates were assembled in an attempt to produce identical cells for comparison. Normally each masterplate would contain five identical cells. This presents the possibility to vary the electrolytes and/or the solvents as the need may be.

The following method was used in this order for the assembly of the master plates.

1. 100 x 100 mm glass plates with ITO ($8\,\Omega$/square) were used.

2. The holes were drilled by a private company prior to printing of the Pt.

3. The half-cells were cleaned in alcohol to remove any residual dirt that accumulated during the handling.

4.   The TiO$_2$ was printed onto the working electrode with a semi automatic screen-printing machine.

5.   The silver (current collectors) on the electrodes was printed in a similar fashion.

6.   The platinum was then also printed on the counter electrode.

7.   Annealing was done in a top hat furnace at 450 °C for 45 min.

8.   The electrodes were vacuum lamination with two layers (for better sealing) of Surlyn 1702 hot melt.

9.   The dye was introduced after sealing by circulating a solution of the dye through the cells at 40 °C with a circulation pump.

10. The cells were rinsed with dry alcohol and dried.

11. The electrolyte was introduced with similar equipment that was used for the dye circulation.

12. The holes were sealed with a specially designed hot press. Surlyn 1702 was used as sealant and the hole was covered with a square (8x8x1.2 mm) glass cover.

13. Electrical wires were attached to all the cells by soldering it to the silver current collectors on the two electrodes and sealed with epoxy glue.

The results of the characterisation of these cells are presented in Chapter 6.4.

4.3 Analytical techniques

4.3.1 UV-vis

A Perkin Elmer, Lambda 750S UV/Vis spectrometer was used to obtain the UV/Vis reflectance and absorbance spectra as part of the characterisation of the cells. The shift and intensity of the absorption band at 540 nm due to reverse bias was investigated.

Scan range: 190 to 800 nm

Scan rate: 266.7 nm/min

Resolution: 1 nm

4.3.2 FT-IR measurements

The FT-IR spectral data were collected on a Perkin Elmer Spectrum 100 FT-IR spectrometer interfaced with a Spectrum Spotlight 400 FT-IR imaging system. The changes in the N-C-S vibration band at 2100 cm^{-1} and C=O vibration bands at 1715 and 1354 cm^{-1} were monitored.

Scans per sample: 64

Resolution: 4.00 cm^{-1}

Mode: attenuated total reflectance (ATR)

4.3.3 Raman measurements

The Raman signal is characteristic of a particular functional group. This function would enable the degradation of the dye in the cell during reverse bias (Gao *et al*., 2007) to be studied. Raman spectroscopy finds applications in identifying organic compounds containing non-polar bonds such as carbon - carbon double bonds or aromatic rings (weak dipoles). Raman spectra were

obtained with Jobin Yvon Lab Ram HR800 spectrometer at room temperature, and samples were excited using the 514.5 nm line. The spot size was 150 µm and the laser power was 2 mW. The acquisition time per sample was 60 s. The microscope magnification was 10x and the system was interfaced with an Olympus BX 41 camera. The three characteristic vibration bands at 1472, 1540 and 1610 cm^{-1} were used to indicate changes in the Ru – bipyridyl bonds.

4.3.4 SEM measurements

Particle and surface morphologies were studied by scanning electron microscopy using a JEOL JSM 7500F Field Emission Scanning Electron Microscope. The nano TiO_2 that was synthesised in our laboratories was compared with the P25 that was obtained from Degussa, South Africa. The surfaces of the cells were compared before and after the reverse bias experiments.

4.3.5 Efficiency measurements

Various cells (at least five of each) were assembled to assure repeatable results of the tests. The current-voltage (I-V) characteristics of the solar cells were monitored and recorded with the use of a mobile testing station for photovoltaics (MTSP purchased from Dyesol, Australia) and the solar simulator was obtained from Sciencetech (USA). The cells were scanned from -0.1 V to 0.8 V and plotted against the current. All measurements were done under irradiation of 1 sun (1 kWm^{-2}).

4.3.6 Impedance measurements

A series of cells were prepared to determine the different effects and contributors inside the cell. All cells were filled with electrolyte.

Figure 4.2 is a diagram of the different cells that were used for the abovementioned experiments.

The following combinations were assembled:

a. TCO-glass only,

b. TCO-glass with Pt counter electrode,

c. TiO_2 only plus counter electrode with Pt and

d. TiO_2 plus dye plus counter electrode with Pt (complete cell).
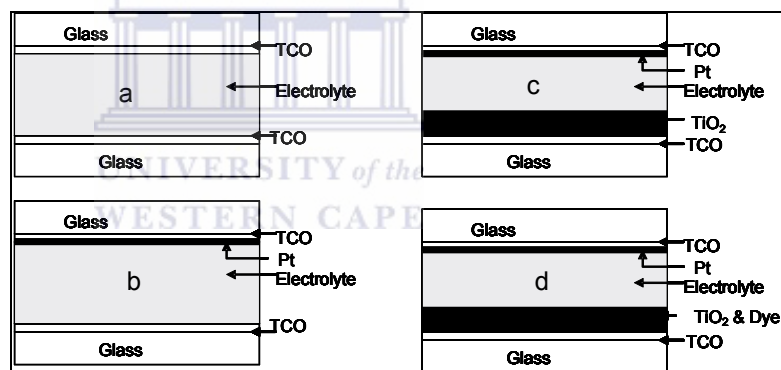
Figure 4.2: Cells that were constructed for the initial impedance measurements.

The electrochemical (impedance and cyclic voltammetry) measurements were carried out using a PGSTAT 12/30/230 potentiostat. A two electrode configuration was used where the sensitised TiO_2 was connected as the working electrode while the counter electrode (Pt), doubled as the reference electrode. The scan rate was 50 mV/s. The bias potentials ranged from -0.7 V to +0.7 V.

4.3.7 Cyclic voltammetry

Voltammograms were generated by using a scan rate of 50 mV/s and the respective ranges of (-1 V to 1 V) and (-0.2 V to 0.4 V).

The measurements were repeated after the reverse bias experiments to determine the effects on the redox reactions.

4.3.8 Laser Beam Induced Current (LBIC)

The wavelength of the diode used as the laser source was in the range of 633–680 nm. The diameter of the laser exit aperture was 600 μm that yielded a power density of 0.4 W/cm². The measurement interval distance was 400 μm. Two bi-polar stepper motors were used to drive the *x–y* stage and interfaced to the digital outputs of a PCI-703 data acquisition board (Gxasheka *et al*., 2005).

4.3.9 Reverse bias and recovery

Cells with an area of 4 cm^2 were subjected to different reverse bias (see Figure 4.3) potentials (1V, 2V, 2.5V and 4.5V). In each case the efficiencies were measured to determine the degree of degradation. The results of the efficiencies vs. time were plotted in Figure 6.12.

A cell was subjected to a reverse bias potential of 2 V and the efficiency was measured at different time intervals to determine the rate of degradation. The regeneration was measured against time after the reverse bias voltage was removed. The efficiencies were plotted against time (see Figure 6.13).
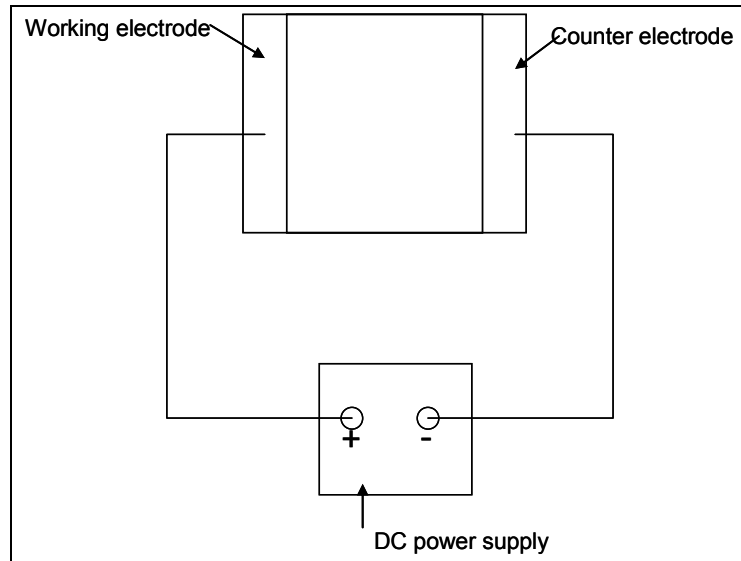
Figure 4.3: Setup for reverse bias experiments (time vs. efficiency)

4.3.10   Equivalent circuits and resistance comparison

Nyquist plots were used to derive equivalent circuits for the different bias experiments. The impedance values were compared with that of the Bode plots as well as the IV curves.

CHAPTER 5

5 CHARACTERISATION AND MEASUREMENTS

5.1 Efficiency measurements/calculations

5.1.1 Air mass 1.5

The air mass coefficient is a reference that indicates the absorption of the solar radiation after it has traveled through the atmosphere (Figure 5.1). For a thickness L_o of the atmosphere, the path length L through the atmosphere for solar radiation at an angle θ relative to the normal to the Earth's surface is:

$$L = L_o / \cos \theta \qquad \textit{equation 5.1}$$

The ratio L / L_o is the air mass coefficient (Würfel, 2005). The solar spectrum outside the atmosphere is at AM0. The spectrum on the surface of the Earth for normal incidence is at AM1. It is agreed that the standard spectrum used in the characterisation of solar cell efficiencies is at AM1.5, which corresponds to a solar zenith angle of 48.2°. (ASTM: Terrestrial Reference Spectra for Photovoltaic Performance Evaluation) (http://rredc.nrel.gov/solar/spectra/am1.5. 2005)
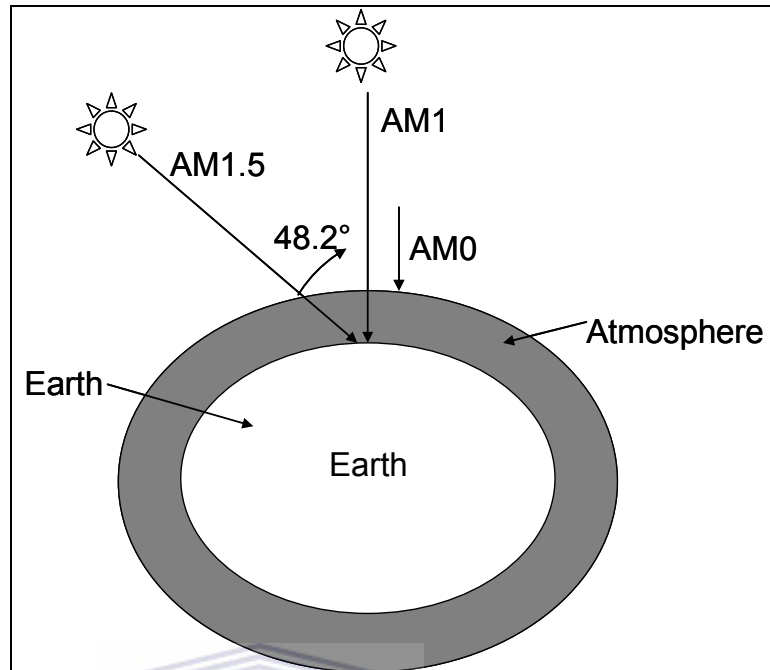
Figure 5.1: Spectral power distribution indicating AM1.5

5.1.2 IV-curves

When a DSC is illuminated, the current through the solar cell is offset by an amount equal to the photo-current I_{ph}, caused by the electron injection of the dye into the conduction band of the TiO_2. An example of an IV-curve is shown in Figure 5.2. In order to normalise results of the cells with different areas, the current density (J = I/area) is used rather than the current (I). The performance of the cell (η = energy efficiency) is represented by the open-circuit voltage V_{oc}, defined as the voltage supplied by the cell when there is no external connection between the electrodes, i.e. the total current is zero. The short-circuit current density J_{sc}, is defined as the current density if the two electrodes are short circuited, i.e. the voltage across the cell is zero, and the fill factor FF, defined as the squareness of the IV-curve (ratio between the maximum power output P_{max} and the product of V_{oc} and J_{sc}); i.e.

$$FF = \frac{P_{max}}{J_{sc}\,V_{oc}} = \frac{J_{max}\,V_{max}}{J_{sc}\,V_{oc}} \qquad \textit{equation 5.2}$$

Finally, the energy-conversion efficiency, η, is defined as the ratio of the power output of the cell to the power input of the incoming illumination P_{input}, and is given by:

$$\eta = \frac{P_{max}}{P_{input}} = \frac{V_{OC}\,J_{SC}\,FF}{P_{input}} \qquad \textit{equation 5.3}$$
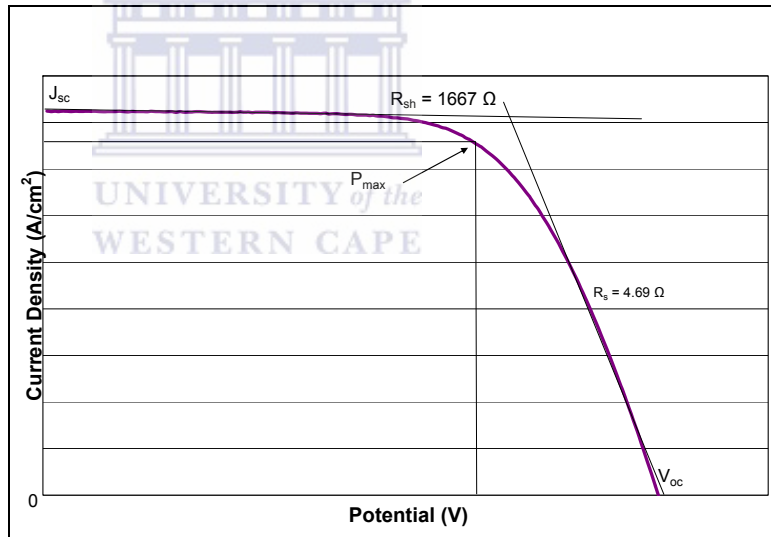
Figure 5.2: A typical IV curve for the determination of the cell efficiency.

The sum of all the ohmic parallel resistance is the shunt resistance (R_{sh}) (Junghanel 2006).
The shunt resistance (R_{sh}) describes the recombination of the electrons from the TiO_2 electrode to the electrolyte.

Nusbaumer (2004) showed that the inverse of the slope of the tangent line at I_{sc} represents the R_{sh}, while the inverse of the slope of the tangent line at V_{oc} represents R_s.

5.1.3 The Butler-Volmer and diode equations for the characteristics of the IV curve.

The Butler–Volmer equation is used to describe the relationship between electron transfer rate and potential (Bard, 1980).

Sastrawan *et al.,* (2006), describes the usefulness of the Butler-Volmer equation and variations.

The one-diode model can be used to describe the IV curve in forward bias by the following equation:

$$J(V) = J_{sat}\left(\exp\frac{qV - qR_sJ(V)}{nkT} - 1\right) + J_{sc} + \frac{V - R_sJ(V)}{R_{sh}} \qquad equation\ 5.4$$

The Butler-Volmer equation generally describes the charge transfer over a metal/electrolyte interface, which is not determined by diffusion limitation in the electrolyte. Then the charge transfer only depends on the applied potential.

The Butler-Volmer model is only valid in reverse bias. (Hinsch *et al.*, 2006). J_0 is the exchange current density. β is the skewness factor with a value between 0 and 1. The closer that β get to 0.5 the more symmetrical the curve is. In reverse bias (V<0), the first exponential term may be neglected and under forward bias (V>0) the second exponential term does not contribute to the current density:

$$J(V) = J_0\left(\underbrace{\exp\left(\beta\frac{qV}{kT}\right)}_{\sim 0\ for\ V < 0} - \underbrace{\exp\left(-(1-\beta)\frac{qV}{kT}\right)}_{\sim 0\ for\ V > 0}\right)$$

44

equation 5.5

Therefore the complete model to describe the shape (Figure 5.3) of the IV curve of a DSC over the full voltage range can be written as (equation 5.6, Hinsch *et al.*, 2006).

$$J(V) = \underbrace{J_{sat}\left(\exp\frac{qV-qR_sJ(V)}{nkT} - 1\right) + J_{sc} + \frac{V-R_sJ(V)}{R_{sh}}}_{\text{one diode model}} - \underbrace{J_0 \exp\left(-(1-\beta)\frac{qV}{kT}\right)}_{\text{Butler-Vollmer model}}$$

Forward bias   Reverse bias
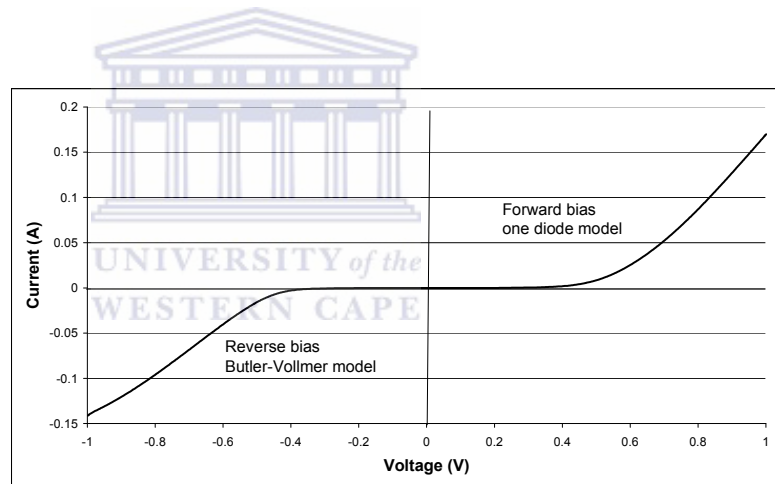
Figure 5.3: An example of a typical DSC IV curve over the positive and negative voltage range.

5.2 Impedance

5.2.1 Theoretical Modelling of the Frequency Response

Electrochemical impedance spectroscopy (EIS) is a useful method for the overall evaluation of the DSC. By using Nyquist and Bode plots, valuable information regarding the charge transfer resistance, diffusion, etc. inside the cells can be gathered. Impedance can be expressed as a

complex number, where the resistance is the real component and the combined capacitance and inductance is the imaginary component.

Electrochemical impedance is usually measured by applying an AC potential to an electrochemical cell and measuring the current through the cell (Karden, 2000). The response to this potential is an AC current signal. This current signal can be analysed as a sum of sinusoidal functions (a Fourier series).

The excitation signal can be expressed as a function of time:
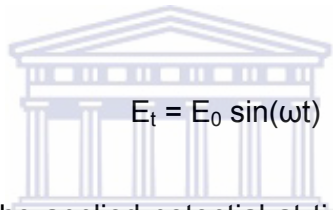
$$E_t = E_0 \sin(\omega t)$$ *equation 5.7*

E_t is the applied potential at time t, E_0 is the amplitude of the signal (maximum voltage), and ω is the radial frequency. The relationship between radial frequency ω (radians/second) and frequency f (hertz) is:

$$\omega = 2\pi\, f$$ *equation 5.8*

In a linear system, the current response signal, I_t, is shifted in phase (Φ) and has a different amplitude, I_0.

$$I_t = I_0 \sin(\omega t + \Phi)$$ *equation 5.9*

By using an expression that is analogous to Ohm's Law, the impedance of the system can be calculated.

$$Z = \frac{E_t}{I_t} = \frac{E_0 \sin(\omega t)}{I_0 \sin(\omega t + \Phi)} = Z_0 \frac{\sin(\omega t)}{\sin(\omega t + \Phi)}$$

equation 5.10

The impedance is therefore expressed in terms of a magnitude, Z_0, and a phase shift, Φ.

The DSC contains three spatially separated interfaces formed by ITO/TiO_2, TiO_2/electrolyte, and electrolyte/Pt-ITO. (See Figure 2.5). Wang *et al.,* (2005) explains that the electron transfer is coupled to electronic and ionic transport. Under forward bias and in the dark, electrons are injected in the conduction band of the TiO_2 nanoparticles and their motion is coupled to that of I^-/I_3^- ions in the electrolyte (Hoshikawa *et al*., 2006). Under illumination additional redox processes at the TiO_2/dye/electrolyte interface take place comprising sensitised electron injection, recombination with the parent dye, and regeneration of the sensitiser. During photovoltaic operation, this "internal current generator" drives all the electronic and ionic processes in the solar cell (Pitarch *et al*., 2004). Impedance spectroscopy looks at the frequency response at the *different interfaces*.

5.2.2 Impedance of different components in an electrical circuit

Impedance is the general term for the ratio of voltage to current. Resistance is the impedance value when $\Phi = 0$ (Φ is the phase difference between the voltage and current), reactance the special case when $\Phi = 90°$. (http://www.physclips.unsw.edu.au/jw/AC.html, 2006.)

Figure 5.4 summarises the impedance of the different components. The voltage on a *capacitor* is always *lagging* the current by 90° while the voltage across an *inductor* is *leading* the current by 90°.
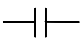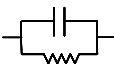
When the frequency is zero in a DC circuit the inductance is a short circuit (impedance is zero) while a capacitor is an open circuit, and therefore the impedance is infinity.
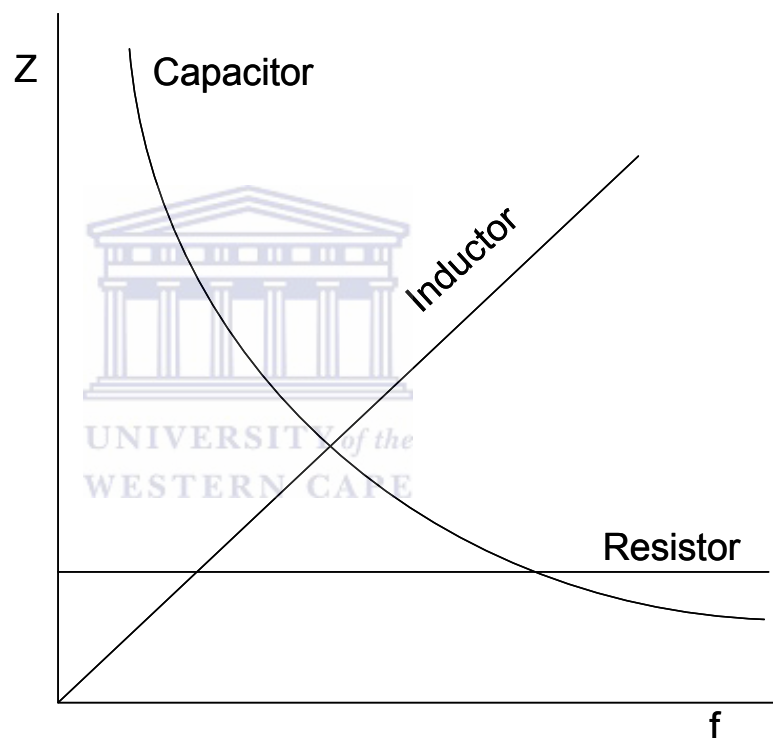
Figure 5.4: The impedance of different components of a cell

The following equations and symbols can be used for the mathematical description of different components.

─┤├─	Capacitor	$Z=0-j/\omega C$
─ww─	Resistor	$Z=R+0j$ $(j=\sqrt{-1})$
─┤├─ └ww┘	Randles cell	$Z=R/(1+\omega^2C^2R^2)-$ $(j\omega CR^2)/(1+\omega^2C^2R^2)$

5.2.3 Data Presentation

Nyquist and related plots are classical methods of assessing the stability of an electrical circuit. The expression for $Z(\omega)$ is composed of a real and an imaginary part. A Nyquist plot is obtained when the real part of the impedance is plotted on the X-axis and the imaginary part on the Y-axis of a chart (see Figure 5.5.). Note that in this plot the y-axis is negative and that each point on the Nyquist plot is the impedance at one specific frequency. The low frequency data are on the right side of the plot and higher frequencies are on the left. The impedance is represented as a vector of length |Z| while the angle between this vector and the X-axis is **Φ** (=arg Z). ω is the angular or radial frequency ($\omega = 2\pi f$ and f = ordinary frequency).

Nyquist plots have one major shortcoming. When a point on a Nyquist plot is examined, it is not possible to tell what frequency was used to record that point.
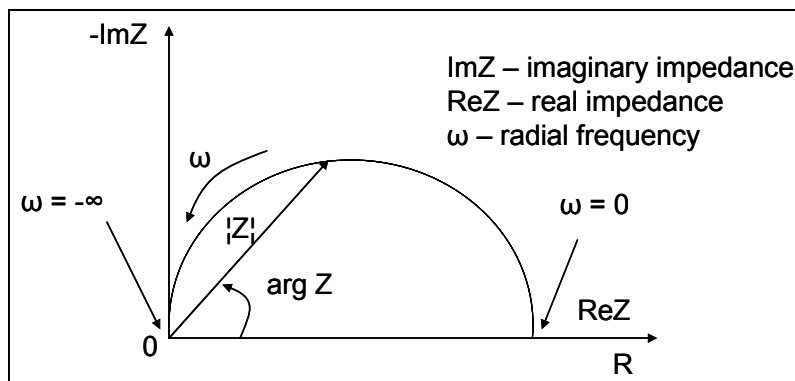
Figure 5.5: Nyquist Plot with Impedance Vector

The semicircle is characteristic of a single time constant. Electrochemical Impedance plots often contain more than one semicircle (Han *et al*., 2006) or often only a portion thereof due to different processes that take place within a cell.

The basic equivalent electrical circuits that are possible during the operation of the DSC is represented in Figure 5.6. Note that this is only basic and the circuit for the different processes in the DSC can be much more complicated. Capacitors can be replaced with constant phase elements. A constant phase element, (Q), in the equivalent circuit, models the behaviour of an electrical double layer which acts an imperfect capacitor. The constant phase is always $-(90*n)°$. The value of n is between 0 and 1. When n=1 then the constant phase element is an ideal capacitor and when n=0 then it is a resistor.

Figure 5.7 gives an example of the Nyquist plot with the different components.

The chemical capacitance accounts for the change in Fermi levels when the dye electrons are excited.

Charge storage is represented by capacitors (reversible energy storage).

Interfacial charge-transfer, transport and recombination are represented by resistances (irreversible process).
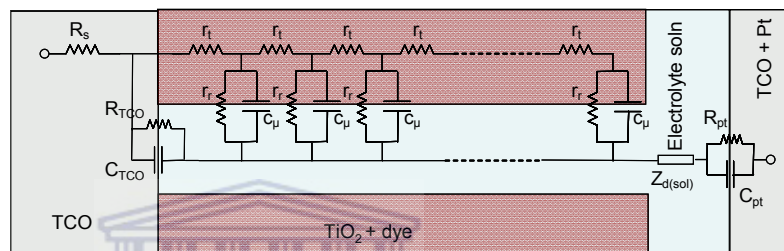
Figure 5.6. Equivalent circuit for a complete DSC (Reproduced from Fabregat-Santiago *et al*., 2005)

- C_μ (=$c_\mu L$) is the chemical capacitance due to a change in electron density.
- R_t (= $r_t L$) is the electron transport resistance in the TiO_2 layer (*L*= film thickness).
- R_r (= r_r/L) is the charge-transfer resistance due to the recombination of electrons at the TiO_2/electrolyte interface also described as the shunt resistance (R_{sh}).
- R_s is the series resistance, mainly that of the TCO.
- R_{TCO} is the charge-transfer resistance for electron recombination from the uncovered layer of the TCO to the electrolyte.
- C_{TCO} is the capacitance at the triple contact TCO/TiO_2/electrolyte interface.
- $Z_{d(sol)}$ is the impedance of diffusion of redox species in the electrolyte.

- R_{Pt} is the charge-transfer resistance at the counter electrode/electrolyte interface.
- C_{Pt} is the interfacial capacitance at the counter electrode/electrolyte interface.

The charge transfer at each of the three interfaces can be described as a Randles cell (Bisquert, *et al.,* 2004, Conference proceedings).
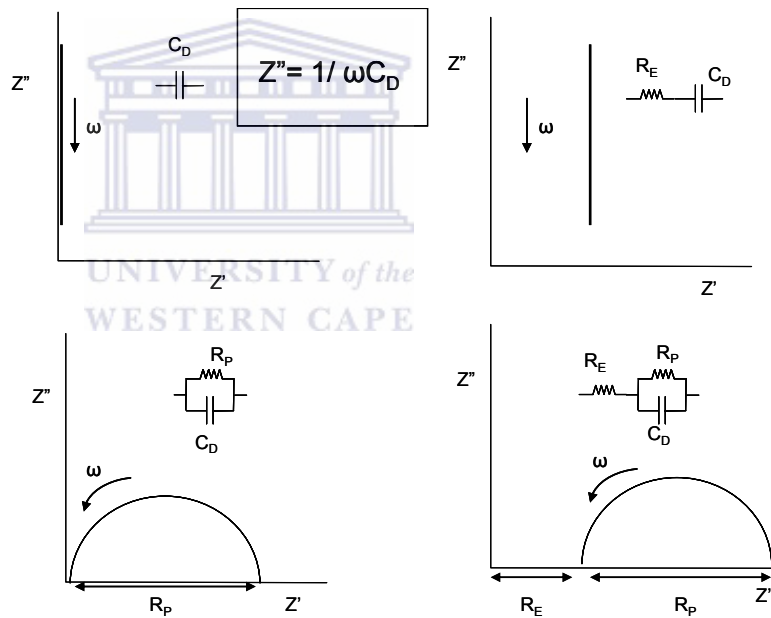
Figure 5.7: Nyquist plots and the equivalent circuit diagrams

(Reproduced from Bisquert, 2004)

Another useful presentation method is the Bode-plot. The impedance is plotted on the y-axis against the log of the frequency on the x-axis. Both the absolute values of the

impedance ($|Z|=Z_0$) and the phase-shift are plotted on the y-axis.
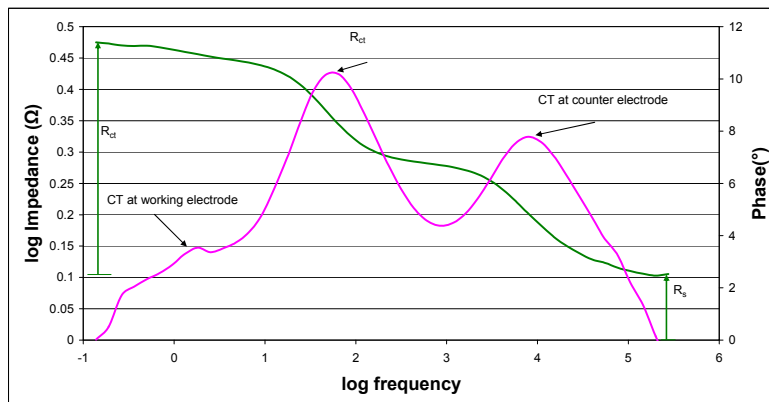
Figure 5.8: a Typical Bode plot in DSCs. The series resistance (R_s) as well as the charge transfer resistance (R_{ct}) of the cell can be determined when the log of the absolute value of impedance is plotted against the log of the frequency (green). Note the three zones on the phase angle plot (pink).

R_s is measured at the maximum frequency or at the frequency where the impedance gives a constant reading at high frequency. In this case the log(f) is between 5 and 6 in figure 5.8.

R_{ct} is measured at the lowest frequency and is usually also the part of the graph where the impedance is levelling off.

Unlike the Nyquist plot, the Bode plot contains frequency information. Bode plots are a very useful way to represent the impedance gain and phase of a system as a function of frequency. This is referred to as the frequency domain behaviour of a system. (http://www. swarthmore.edu/ NatSci/echeeve1/Ref/ LPSA/Bode/ Bode.html. 2006).

When the frequency is plotted against the impedance (phase angle plot), there is a possibility of three characteristic peaks (Figure 5.8) observed in the spectra of DSCs which could be identified (in order of increasing frequency) by:

- Diffusion in the electrolyte (Nernst diffusion).

- The recombination of electrons from the conduction band of the TiO_2 by the I_3^- interface diffusion and electron transfer in the TiO_2 (working electrode).

- The electron charge transfer at the platinum counter electrode (see Figure 5.8).

Figure 5.9 is an illustration of parallels between Nyquist plots and Bode plots.
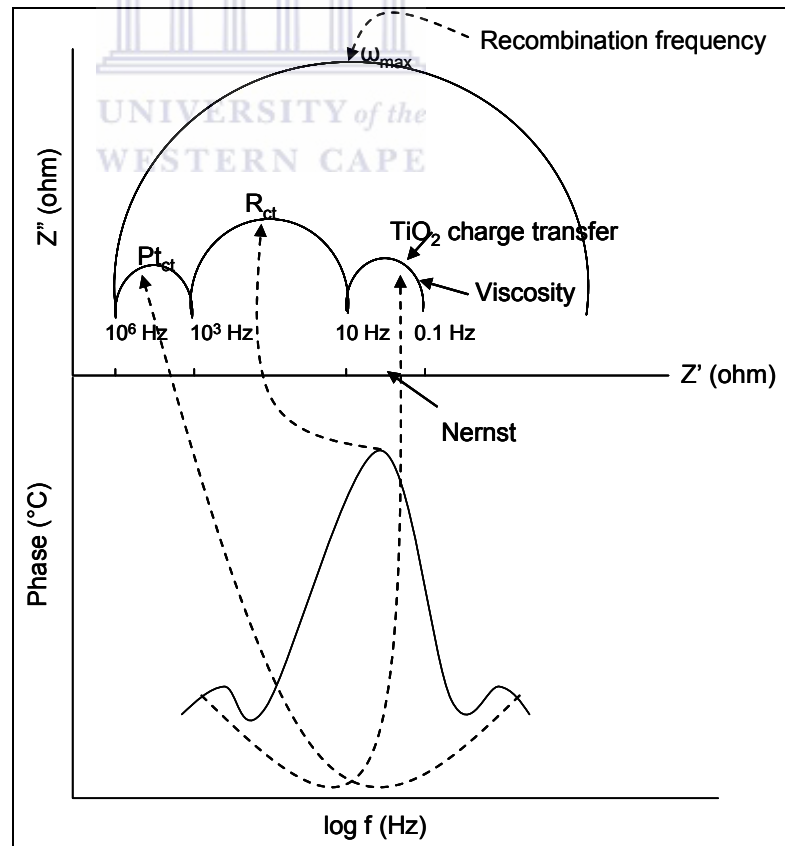
Figure 5.9: Diagram that shows the relation between the different areas in the Nyquist and Bode plots

If the Bode plot exhibits three peaks then the Nyquist plot will have three semi circles. Although the frequency is not indicated on a Nyquist plot, each activity that is characteristic for each semi circle falls in a specific frequency range. The frequency range of 10^6 to 10^3 is typical for the charge transfer resistance at the platinum electrode while the low frequency range (10 to 0.1 Hz) represents the charge transfer at the TiO_2 electrode which also incorporates viscosity and Nernst diffusion resistance. The intermediate frequency range, which is usually the major of the three semi circles, represents the charge transfer due to recombination reactions in the cell.

5.3   Cyclic voltammetry

Cyclic voltammetry (CV) is one of the most versatile electroanalytical techniques when it comes to study of electroactive species, since it is relatively easy to use and gives a good overview of the redox reactions and the kinetics of the reactions that occur within a certain potential range. Characteristics such as charge accumulation, charge transport, and interfacial charge transfer can be translated into simple electrical equivalents (Fabregat-Santiago *et al.,* 2003). A cyclic voltammogram is recorded by cycling the potential of the working electrode while the resulting current is measured. This gives the potentials at which charge transfer reactions take place and indicates if they are reversible or not. In Figure 5.10 it is shown how the current varies with a change in potential for a reversible redox couple.

The formula that forms the base of the calculations is the Nernst equation:

$$E = E^{\circ\prime} + \frac{RT}{nF} \ln\left[\frac{C_{ox}}{C_{red}}\right]$$

5.11

where: E = electrode potential

E°' = standard electrode potential

R = universal gas constant (8.314510 J K^{-1} mol^{-1})

T = temperature in Kelvin

n = number of electrons transferred in the half reaction

F = Faraday constant (9.6485309*10^4 C mol^{-1})

A cyclic voltammogram reflects the reactions occurring at the electrode surface as the potential is cycled. The concentration ratio of C_{Ox}/C_{red} will change when the potential on the working electrode is changed. Thus, when the potential is scanned towards more positive values, an oxidation reaction, *Red → Ox + ne⁻*, will occur as the potential approaches the formal electrode potential *E°'*. This will give rise to an anodic current that increases until the amount of the reductive form of the redox couple at the electrode surface is depleted which will cause the current to decrease, resulting in a peak in the anodic current. When the potential is scanned towards negative values, the opposite will occur at the surface, *Ox + ne⁻ → Red*, which gives rise to a cathodic current.

A two-electrode system was used to do the measurements on the DSC. In this configuration the Pt counter electrode doubled as the reference electrode. Impedance measurements were performed using an Autolab PGSTAT12/30/230 potentiostat.
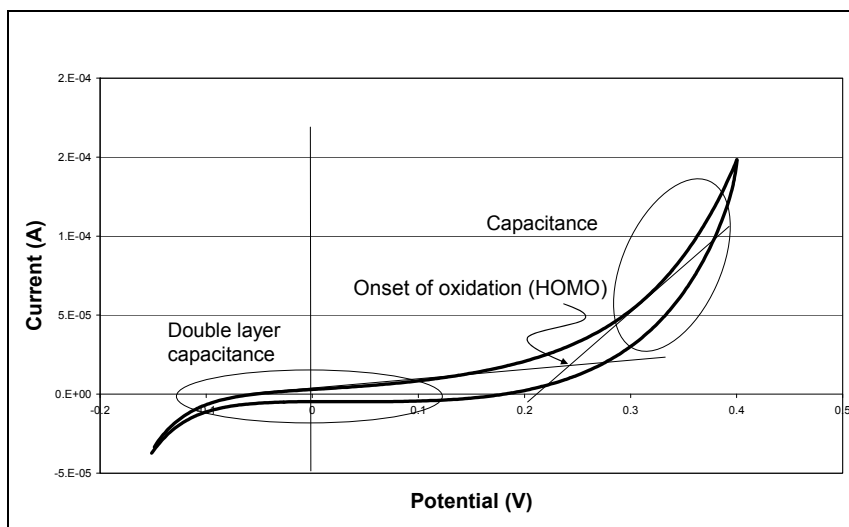
Figure 5.10: An example of a cyclic voltammogram.

Cyclic voltammetry measurements can be used to determine the highest occupied molecular orbital (HOMO) and lowest unoccupied molecular orbital (LUMO) levels of the nanoparticles. The oxidation is in the positive potential region and the reduction of the neutral species is in the negative potential region.

Double layer capacitance is indicated by the difference in current between the forward and backward sweep (opening of the two lines) before any sharp change in the current. A double layer is formed at the interface and little or no charge transfer takes place. This area is indicated in Figure 5.10. When a voltage is applied to the cell, and the current increases, capacitance behaviour is indicated (Fabregat-Santiago *et al.,* 2005). As a result of the high concentration of the iodide species in the DSC, there was no clear decrease in the current due to depletion of the reductive form of the electrolyte. This resulted in a smooth voltammogram.

5.4 Raman spectroscopy

A laser beam is directed to the sample and the scattered radiation is collected. Most of the scattered radiation has the same wave number as that of the incident laser beam while a fraction will have a different wave number. The signal is amplified and captured by a photo detector. This is the Raman signal and is characteristic of a particular functional group. Raman spectroscopy finds applications in identifying organic compounds containing non-polar bonds such as carbon – carbon double bonds or aromatic rings (weak dipoles).

When the light from a molecule is scattered, most of the photons are *elastically scattered*. Raman spectroscopy is the measurement of the wavelength and intensity of *inelastically scattered* light from these molecules (Kaiser optical systems, http://www.kosi.com, 2005). Although most instruments use a single frequency of radiation to irradiate the sample it is possible to obtain instruments that can do a range of wavelengths from 1260 to 1700 nm. In Raman spectroscopy, only transitions where the polarisability of the molecule changes are observed.

Raman and IR spectra provide complementary information for the study of molecular vibrations and structure. Typical applications are in structure determination, multi-component qualitative analysis, and quantitative analysis.

Resonance Raman (RR) spectroscopy
This aspect of Raman spectroscopy becomes especially useful for large biomolecules with chromophores embedded in their structure. In such chromophores, the charge-transfer (CT) transitions of the metal complex generally enhance metal-ligand

stretching modes, as well as some of modes associated with the ligands alone. The main advantage of RR spectroscopy over traditional Raman spectroscopy is the large increase in intensity of the peaks in question (by as much as a factor of 10^6).

Difference between Raman and IR spectroscopy

In Raman spectroscopy, the incoming photon causes a momentary distortion of the electron distribution around a bond in a molecule, followed by emission of radiation as the bond returns to its normal state. This causes temporary polarisation of the bond, and an induced dipole that disappears upon relaxation. In a molecule with a centre of symmetry, a change in dipole is accomplished by *loss of the centre of symmetry*, while a change in polarisability is accomplished by *preservation of the centre of symmetry*. Thus, in a centrosymmetric molecule, *asymmetrical* stretching and bending will be IR active and Raman inactive, while *symmetrical* stretching and bending will be Raman active and IR inactive. For molecules without a centre of symmetry, each vibrational mode may be IR active, Raman active, both, or neither. Symmetrical stretches and bends, however, tend to be Raman active.

5.5 Fourier Transform Infrared radiation (FTIR)

Infrared radiation is focussed directly onto the sample, and the intensity of the transmitted light is compared with that of the incident light. A reduction in intensity at a given wavelength of light indicates the absorption of energy by a vibrational transition. The energy, *E*, of a photon is $E = h\nu$, where *h* is Planck's constant and ν is the frequency of the radiation. The

energy required for such a transition can therefore be calculated if the frequency of the incident radiation is known.

A transition only occurs when a particular vibration causes a net change in dipole moment of the molecule.

5.6 X-ray diffraction

When X-rays interact with a crystalline substance it gives a diffraction pattern. This pattern is unique for each different compound even for a mixture of substances. The substances can be identified from a database called the International Centre Diffraction Data (ICDD). This database can be obtained directly from ICDD or from the instrument supplier.

X-ray diffraction is one of the most important characterisation tools used in solid-state chemistry. It can be used in two main areas, for the fingerprint characterisation of crystalline materials and the determination of their structure as well as the particle size of the sample. The broadening of peaks in the diffraction patterns is indicative of a decrease in the particle size. Each crystalline solid has its unique characteristic X-ray powder pattern which is then used as a fingerprint for its identification.

The atomic planes of crystals appear to reflect X-ray beams at certain angles of incidence θ (see Figure 5.11). The variable d is the distance between atomic layers in a crystal, and the variable lambda λ is the wavelength of the incident X-ray beam and n is an integer. By using the reflection geometry and applying trigonometry, Bragg's law can be derived in terms of the above:

$$n\lambda = 2d\,\sin\theta \qquad\qquad 5.12$$

d (interplanar spacing between the atoms in the crystal)
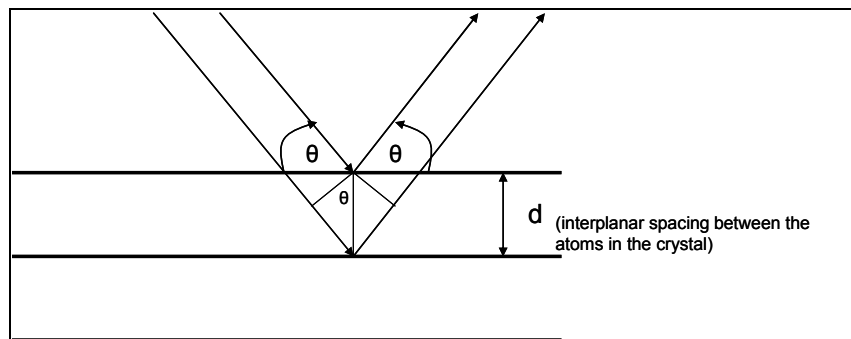
Figure 5.11: X-ray path through a crystal

5.7   UV/Vis and band gap determination

The absorption spectra of the dyes were measured using a Perkin-Elmer UV-Vis light spectrometer.

The absorption maximum of 533 nm is attributed to the metal to ligand charge transfer of the hydroxylated bipyridyl groups of the N3 dye. When two of the carboxylate groups are reacted with TBA to form the N719 dye (see Figure 2.8), the absorption peak at 533 nm moves to higher energy at 530 nm and the absorption peak at 393 nm moves to 387 nm.
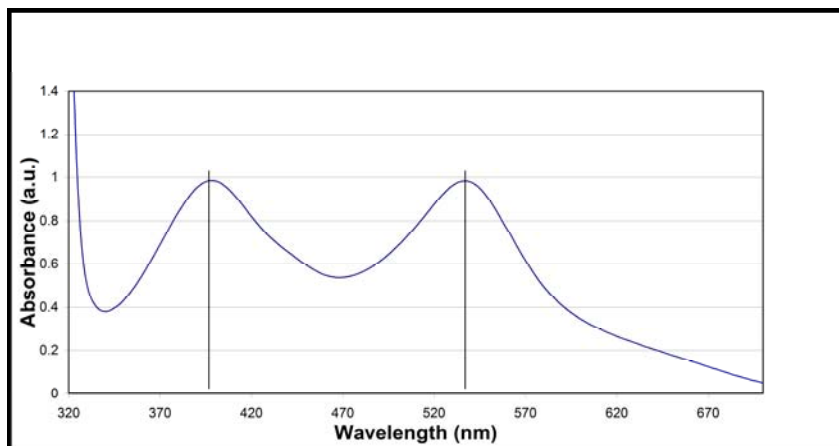
Figure 5.12: The absorption spectrum of the N719 dye complex

Theoretically transition could occur from various occupied to unoccupied levels, but in reality, excitation occurs between the two lowest energy transitions, the outer electron, π -> π* and the η -> π* levels for the energy range of 200-800 nm associated with UV-Vis radiation. When the photon is absorbed, a portion of the energy is absorbed as the electron is promoted to the excited state. Figure 5.13 shows the different transitions possible in the dye.
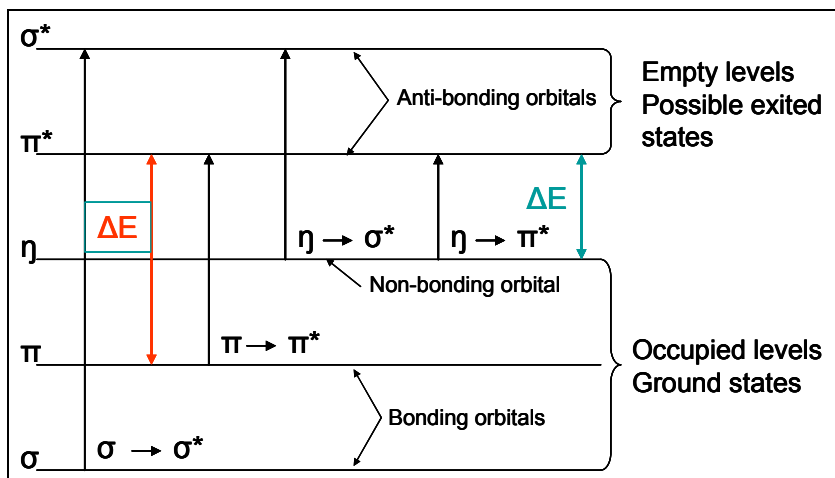
**Figure 5.13:** Electronic excitation of electrons between molecular orbitals

The absorption bands observed in these systems are due to electronic transitions from the ground state to an excited state. During such a transition in a molecule, electrons are excited from the highest occupied molecular orbital (HOMO) to the lowest unoccupied molecular orbital (LUMO) which is analogous to the Fermi level and also the valence band (VB) and conduction band (CB). The band gap is the energy difference between the valence and conduction bands.

The band gap of the TiO_2, can manually be determined by the following procedure.

- The absorbance spectrum is measured from 200 – 900 nm (1.38 – 6.2 eV) and the file is saved in **ASCII** format.
- The absorption coefficient (α) at each wavelength is calculated from:
  α = A/d, where A is the absorbance and d is the film thickness.
- The graph of $\alpha^{1/2}$ vs. E is plotted.
- The curve is extrapolated to α = 0 and the band gap is equal to the x axis where α = 0 (See Figure 5.14). (Stapleton, 2005.)

The relationships as shown in figure 5.14 is given by:

$$\alpha h\nu = A(h\nu - E_g)^{1/2}$$

equation 5.13
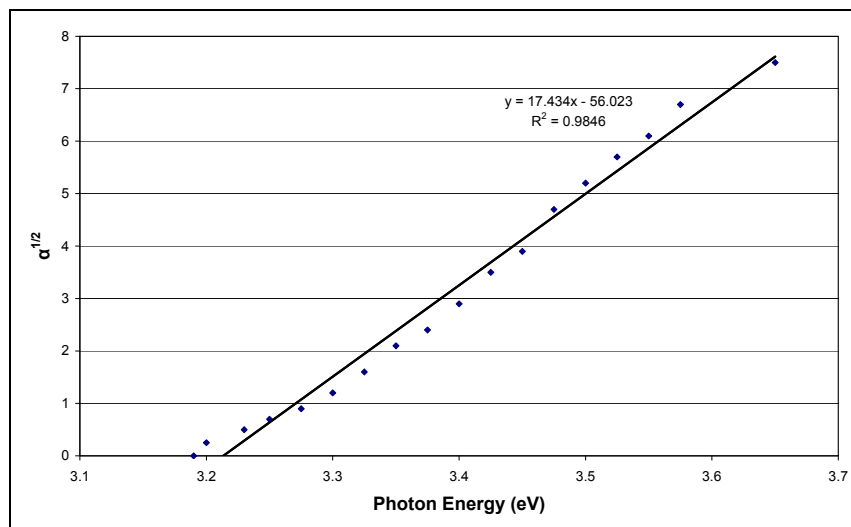
Figure 5.14: Manual method of determining the band gap. This graph was generated from actual laboratory data.

The band gap was determined as 3.22 eV with this method. This value compares favourably with the 3.2 eV for anatase reported in literature (Aarik *et al.*, 1997).

5.8 Scanning Electron Microscope

The scanning electron microscope (SEM) generates a beam of electrons in a vacuum. That beam is collimated and focused by electromagnetic lenses and scanned across the surface of the sample by electromagnetic deflection coils. The interaction of the primary electron beam with the material of the sample in SEM causes excitation of secondary, backscattered, Auger electrons, characteristic X-ray radiation and photons of light.

The primary imaging method is by collecting secondary electrons that are released by the sample.

The secondary electrons are detected by a scintillation material that produces flashes of light from the electrons. The light

flashes are then detected and amplified by a photomultiplier tube.

By correlating the sample scan position with the resulting signal, an image can be formed that is similar to what would be seen through an optical microscope. There are other imaging modes available in the SEM. Backscatter imaging uses high energy electrons that emerge nearly 180° from the illuminating beam direction. The backscatter electron yield is a function of the average atomic number of each point on the sample, and thus can give compositional information.

Specimen current imaging using the intensity of the electrical current induced in the specimen by the illuminating electron beam is used to produce an image (electron beam induced current (EBIC)). It can often be used to show subsurface defects.
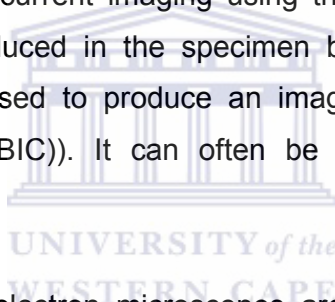
Scanning electron microscopes are often coupled with X-ray analysers. The energetic electron beam - sample interactions generate X-rays that are characteristic of the elements present in the sample and are used to identify local chemical composition of the samples (energy dispersive X-ray spectroscopy (EDS)).

Light luminescence from the sample scanned by electron beam carries information about its electron and defect structure. Detection of this light by photomultiplier and imaging with this signal is called cathodoluminiscence (CL).

Diffraction of backscattered electrons emitted from the surface irradiated by primary beam in SEM is used to investigate

crystallographic properties of samples. Such diffraction patterns are recorded by CCD (charged coupled device) camera or fluorescent screen and are called electron back scattered diffraction (EBSD).

5.9   Laser Beam Induced Current

Laser Beam Induced Current technique is used to obtain high resolution images of DSCs. This technique is widely used in the study of solid-state type solar cells but its use is not so extended on DSCs because of problems arising from the interaction between a focused laser beam and the biphase structure of these devices (Martin *et al.,* 2006). The method used was designed by the department of physics at the NMMU (Nelson Mandela Metropolitan University) for electrical characterisation of the bulk material of the DSC. Cells were subjected to LBIC analysis to determine the short circuit current (I_{sc}) at the spot that the laser activates. I_{sc} is measured in the external circuit and defects in the bulk material can thus be determined. This method was used as a tool for quality control.

CHAPTER 6

6 RESULTS AND DISCUSSION
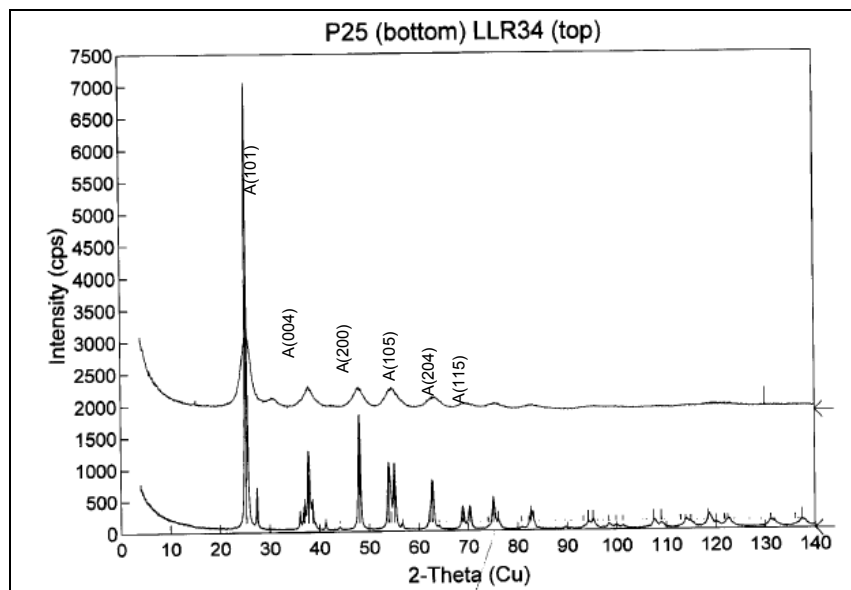
6.1 Nano TiO$_2$

The synthesis of the TiO$_2$ nano particles was successful and yielded an average particle size of 4 nm (± 14.8%) of pure anatase. The following SEM micrograph (Figure 6.1) gives a good indication of the particle size. The XRD results of the product confirmed the particle size (see appendix).

Figure 6.1: SEM micrograph of the CSIR nano particles (LLR 34)

Figure 6.2: XRD of CSIR nano particles (LLR 34) compared with the Degussa P 25

XRD analysis was used to determine the particle size and purity of the nano particles (see Figure 6.2). The particle sizes were compared with each other and determined as 4.0 nm (± 14.8%) for the CSIR nano particles vs. 21.5 (± 12.3%) for the Degussa P 25. The broader peaks of the CSIR sample are an indication of smaller particles. (See appendix for analysis certificate).

Raman results showed no traces of rutile in the final product (Figure 6.3). The appearance of a peak at 440 cm^{-1} would be an indication of the presence of rutile in the sample.
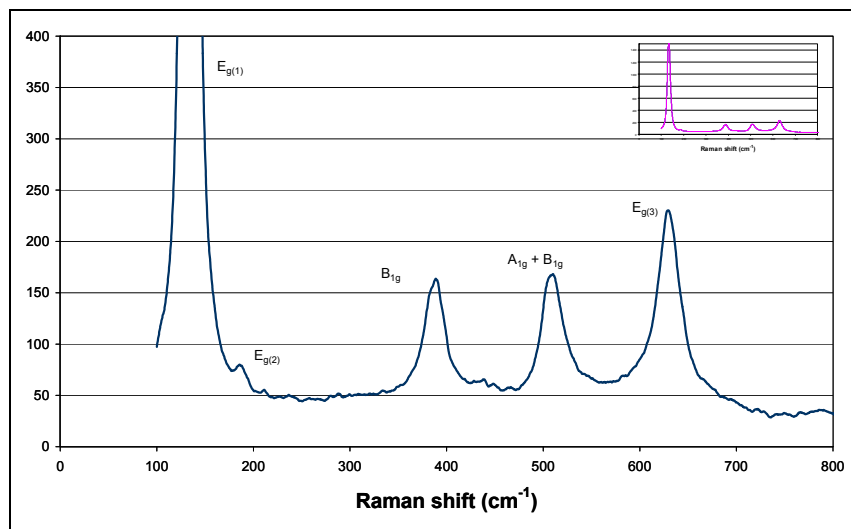
Figure 6.3: Raman spectrum of the nano-TiO$_2$ particles that were produced by the CSIR. The insert gives an indication of the relative peak intensities. Characteristic Raman peaks (Porkodi and Arokiamary, 2007) that corresponded to anatase in the TiO$_2$/ITO sample appeared at 134 (E$_{g(1)}$), 187 (E$_{g(2)}$), 390 (B$_{1g}$), 512 (A$_{1g}$ + B$_{1g}$) and 630 (E$_{g(3)}$) cm^{-1}. Note the absence of the rutile peak at 440 cm^{-1}

6.2 Nano TiO$_2$ paste

It was found that the thin film developed fine cracks as the paste aged (Figure 6.5 and 6.6). The film did not show any changes after annealing. If the paste was seven days old and the thin film then annealed, the film would still have the same morphology after another week. The changes therefore occurred in the paste itself and not on the glass plate after annealing.

The decrease of the peak width in the XRD analysis indicated an increase in the overall particle size in the paste. A stable paste formulation that did not crack after annealing at 450 °C was obtained after experimentation with various ratios of the

Degussa P25 and the CSIR nano particles shown in Figure 6.7. The final formulation of the paste is similar to that of a concrete mixture. The ratio of fine to coarse particles plays a definite role in the strength as well as cracking of the dry product. Without the larger particles the dried paste would crack.
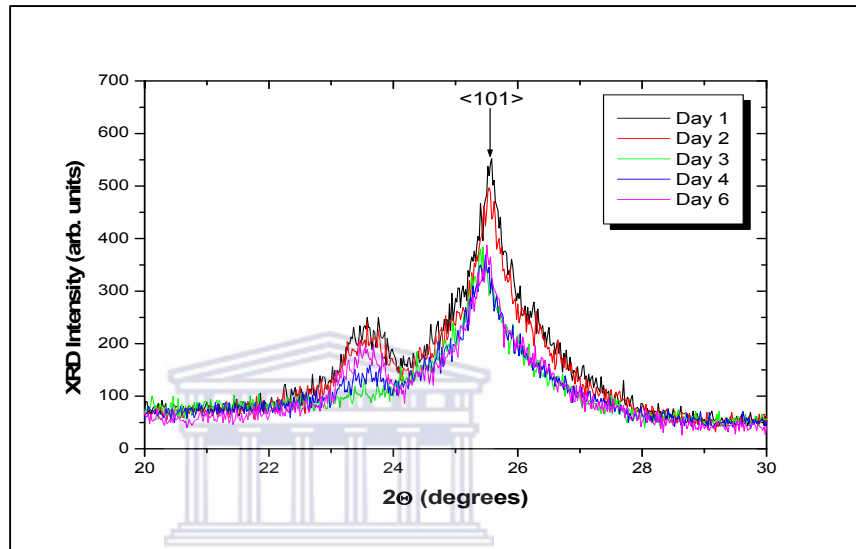
Figure 6.4: XRD results from thin film: The narrowing of the <101> peak after day 2 indicates an increase in particle size
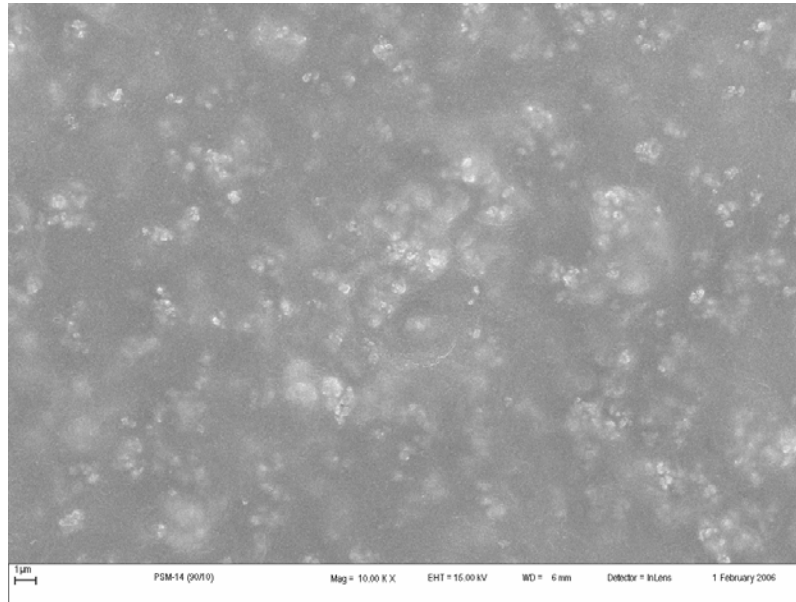
Figure 6.5: SEM micrograph of the film from the paste on day 1
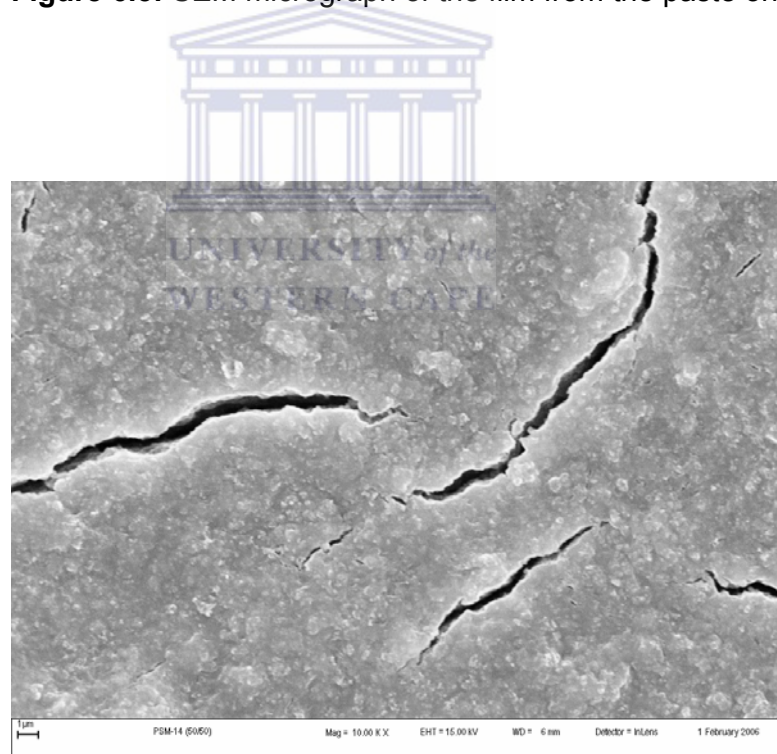
Figure 6.6: SEM micrograph of the cracked film from the paste on day 6
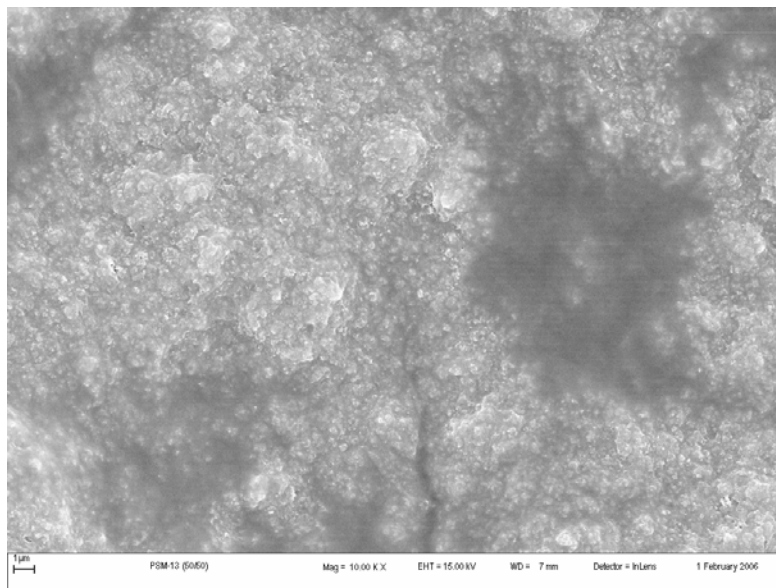
Figure 6.7: SEM micrograph of the film from the paste of the final product

6.3 Single cell construction

The following single cells resulted from the method that is described in chapter 4.2 on page 31.

Figure 6.8: Two printed electrodes for large single cell DSCs. Note the white lines on the electrodes (silver current collectors).

The dimensions of the silver lines were chosen so that a layer of TiO_2 of 8 to 10 mm diameter could be printed between them. This is the norm that is used by ECN in the Netherlands (Sastrawan *et al.*, 2006). The efficiencies of th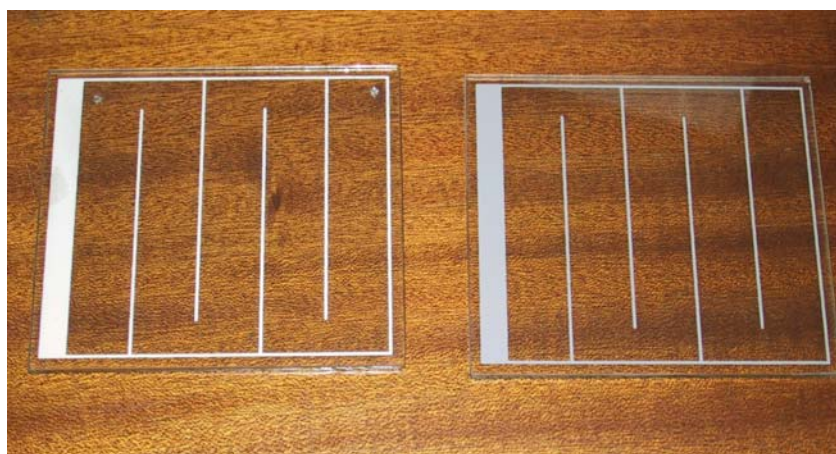ese cells are usually significantly lower (3% vs. 5%) than small cells mainly due to the conductivity of the glass. The areas of these cells are typically 40 cm^2 compared with an area of 2 cm^2 for the small cells. Most of the later research was conducted with small single cells (Figure 6.9) or masterplates (Figure 6.10).
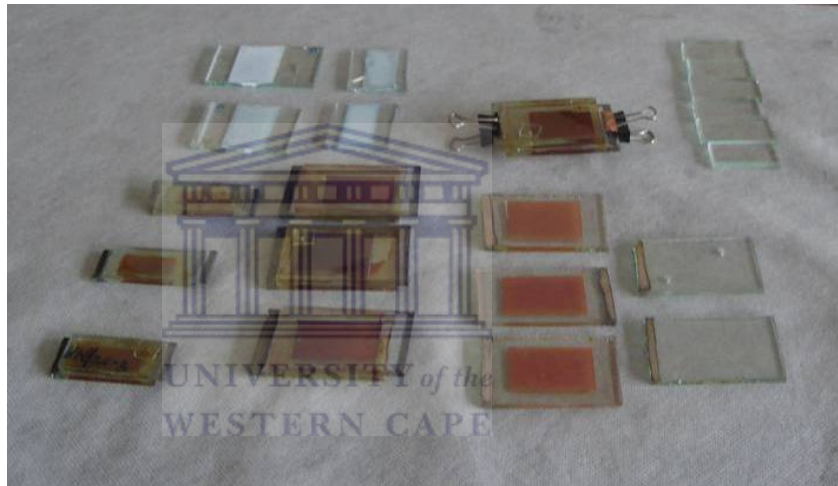
Figure 6.9: Examples of different cells that were assembled for research purposes.

6.4 Master plate assembly

The method for the assembly of masterplates, as described in section 4.3 resulted in cells with the following characteristics.

The following The plate shown in Figure (6.10) was the result of a complete masterplate where each cell was individually characterised. The IV curves of the individual cells are depicted in Figure 6.11. In this case the average efficiency was 5.1% (± 0.1%). The cells were sealed with two layers of Surlyn 1702 for better sealing. This possibly led to a drop in efficiency due to

doubling of the distance between the electrodes. Surlyn 1702 is a low melting polymer (80 to 105 °C) and works well if the glass top is heated with a soldering iron. It softens at 75 °C and is therefore not the long-term answer for sealing.

Figure 6.10: A fully assembled master plate – ready for testing
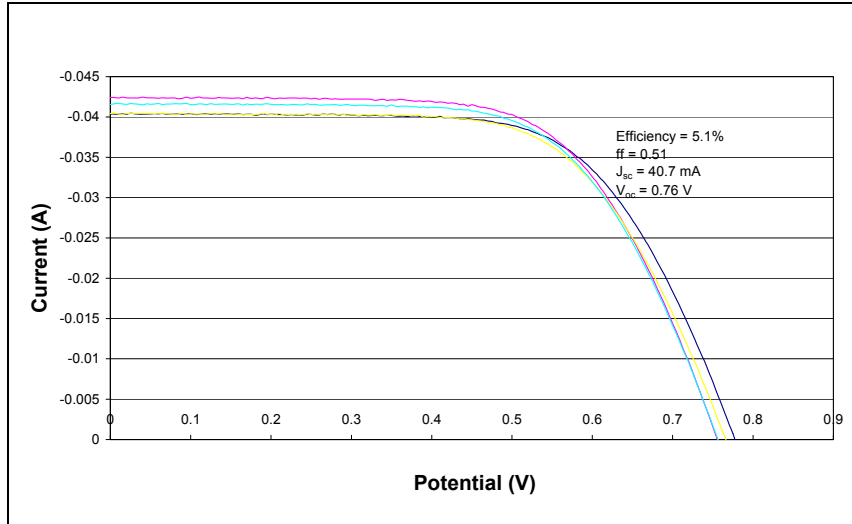
Figure 6.11: IV curves of five individual cells plotted together. The average efficiency was determined as 5.1% (± 0.1%).

The efficiencies were calculated by using the formulae:

$$FF = \frac{P_{max}}{J_{sc} V_{oc}} = \frac{J_{max} V_{max}}{J_{sc} V_{oc}} \quad \text{for the fill factor where}$$

$$J_{sc} = I_{sc}/A \text{ where A is the active area of a cell}$$

and

$$\eta = \frac{P_{max}}{P_{input}} = \frac{V_{OC} J_{SC} FF}{P_{input}} \quad \text{for the efficiency.}$$

The following results (Table 6.1) were obtained for the determination of the efficiencies. The averages are printed in bold. P_{input} was 1 kW/m^2 in all cases and all cells had an active area of 4 cm^2.

Table 6.1: Results obtained from the MTSP that were used to calculate the efficiencies of the cells

Efficiency	FF	I_{sc}	V_{oc}	P_{max}
%	%	mA	V	mW
5.12	65.1	40.4	0.78	20.5
5.17	64.6	42.4	0.76	20.7
5.00	64.6	40.4	0.77	20.0
5.08	64.7	41.6	0.76	20.3
5.09	64.8	41.6	0.76	20.4
5.09	**64.8**	**41.3**	**0.76**	**20.4**

The results of the efficiency measurements of the cells that were used in this case.

6.5 Reverse bias and recovery

The results of four cells (Table 6.2) that were subjected to different reverse bias voltages and the efficiencies were plotted against time are shown in Figure 6.12. The following reverse bias voltages were used in the experiments:

Blue: 1 V; Magenta: 2 V; Black: 2.5 V; Brown: 4.5 V
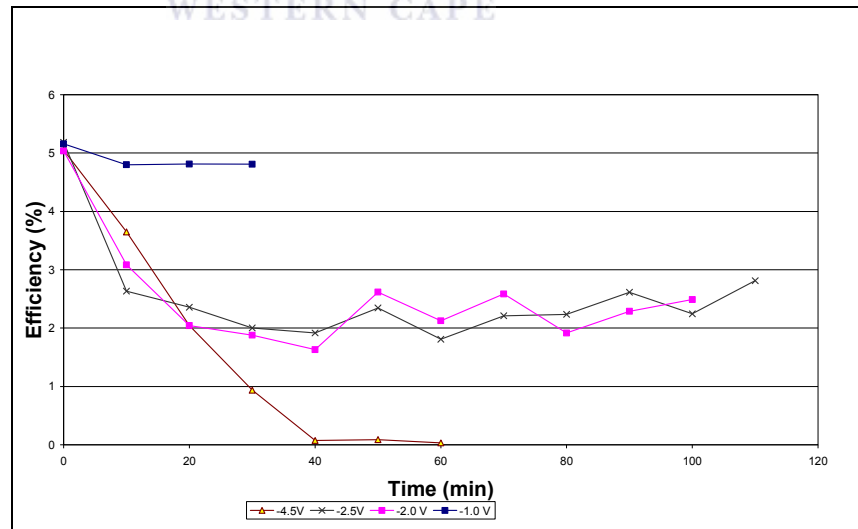
Figure 6.12: Efficiencies plotted during subjection to different reverse bias voltages. Note the similar results for 2 and 2.5 V.

Table 6.2: Average change in efficiencies after reverse bias

Efficiency	1 V	2 V	2.5 V	4.5 V
Start %	5.1	5.0	5.2	5.1
end %	4.8	2.1	2.0	0.07
Difference	5.9	58.0	61.2	98.6

Under a reverse bias of 1 V, there is little reduction in the efficiency of the cell. The drop in efficiency from 5.1 to 4.8% is 0.3% (5.9% overall).

From Figure 6.12 and Table 6.2, it can be seen that there was no meaningful difference when the cells were subjected to reverse bias voltages of 2 and 2.5 V. The results for the 2.5 V reverse bias experiments were therefore not discussed further in this document.

When the cell was subjected to a reverse bias potential of 4.5 V, the efficiency dropped to 0.07% in 50 min. The rest of the work was focussed more on the cells that were subjected to a reverse bias potential 2 V to study the changes inside the cell. The cells that were subjected to a reverse bias potential of 4.5 V were only used as a reference to emphasize the difference between a dead cell and one that has partially recovered. The physical and chemical changes in the dead cell will be covered in future research results.
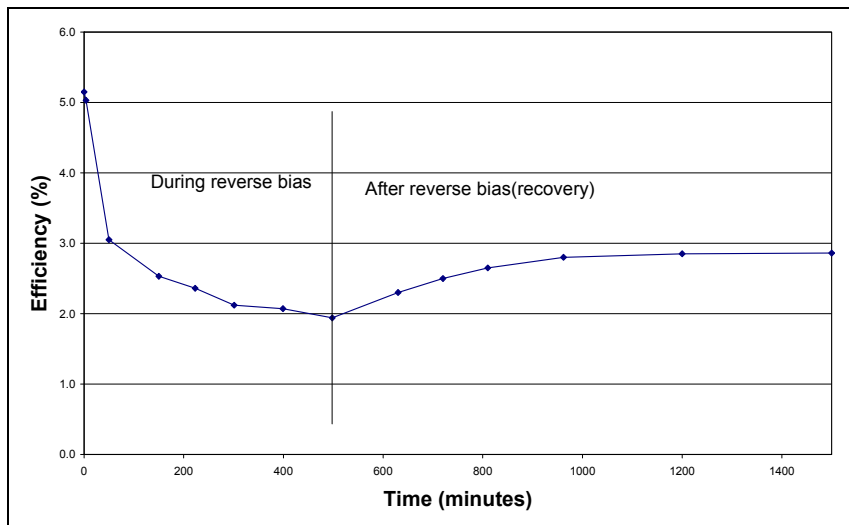
Figure 6.13: A plot of efficiency vs. time for a cell that was subjected to a reverse bias of 2V for 500 min after which the cell's recovery was monitored.

The efficiency of the cell decreased from 5.1% to 2% after 500 min. When the reverse bias potential was removed, the cell recovered partially to give a final efficiency of 2.9%.
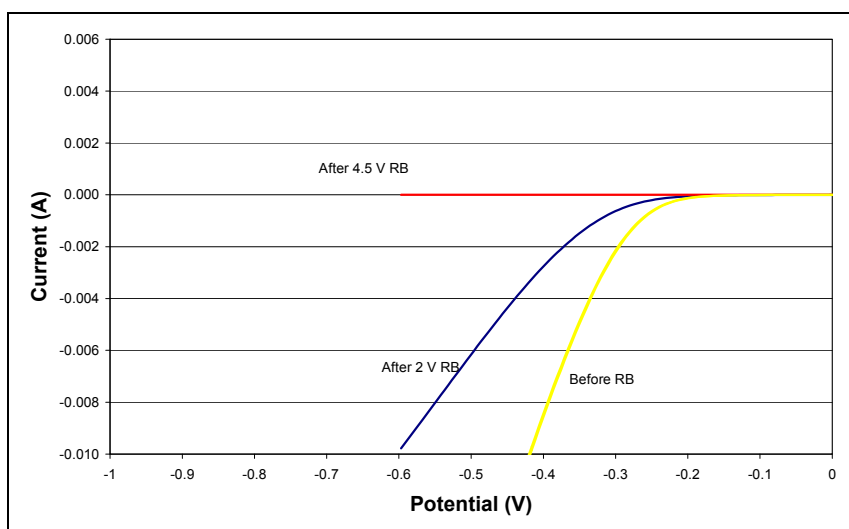
Figure 6.14: The IV curves for the three cells (negative voltages only).

The yellow line represents the cell that was not subjected to any reverse bias. The blue line is the cell that was subjected to 2 V reverse bias while the red graph shows the cell that was subjected to 4.5 V reverse bias.

The data from the graph (Figure 6.14) was used to determine the different values for the exchange current density. Only the Butler-Volmer equation was used for this work because only the reverse bias results were of interest. This was compared with the curve of the cell before reverse bias.

Applying the experimental data to the Butler-Volmer equation (equation 5.6 on page 45), the following graph was plotted for J_0 (exchange current density). To reduce the complexity of the explanation, the symmetry factor (β) was taken as 0.5. J_0 is characteristic of electrode behaviour and is indicative of the rate of oxidation or reduction at an equilibrium electrode. J_0 for the cells were determined as:

Before RB: 8.0×10^{-3} A/cm^2
After 2 V RB: 3.3×10^{-3} A/cm^2
After 4.5 V RB: 3.4×10^{-5} A/cm^2

The reaction rate after the cell was subjected to a reverse bias potential of 2 V was about three times less than the cell before reverse bias. The cell that was subjected to 4.5 V reverse bias had a J_0 value two orders of magnitude less than the initial values before reverse bias.
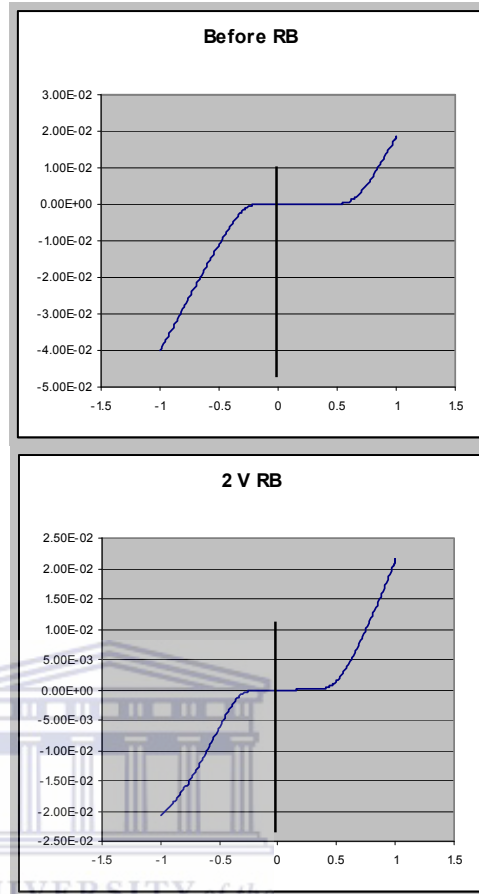
Figure 6.15: Comparison of the shapes of the IV curves for the different cells after the different RB voltages. The voltages are plotted on the x-axis and the current on the y-axis. Note the shift in the breakdown voltages.

The cell that was subjected to 2 V reverse bias shows a slight shift from the zero point and an increase in the breakdown voltage (0.5 to 0.6 V) while the cell that was not subjected to any reverse bias has the largest shift from the zero point. It also has the lowest breakdown voltage of 0.5 V (see Figure 6.15). This is in agreement with Menzies (2007), that an increase in the recombination rate is indicated by a negative shift in the breakdown voltage for the solar cells.

6.5.1 Efficiency measurements
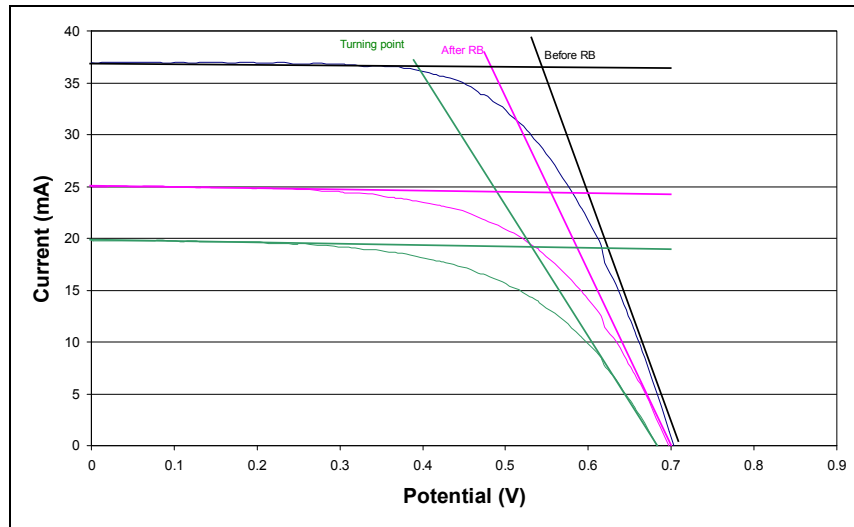
Figure 6.16: IV curves for the cell during and after being subjected to a reverse bias of 2 V. The blue trace is the efficiency before reverse bias while the recovered is indicated by the magenta trace. The green trace represents the turning point before recovery. The slopes of the I_{sc} and V_{oc} are also indicated on the graph.

The IV curves shown in Figure 6.16 were obtained during the time that the cell was subjected to reverse bias. The blue traces are during reverse bias while the recovery is indicated by the magenta traces. Although there was a significant change in the I_{sc}, the V_{oc} showed only a small variation.

The inverse of the slopes of the curve that indicates R_{sh} and R_s are shown in table 6.3.

Table 6.3: Shunt and series resistances as calculated from the I/V-curves

	R_{sh} (Ω)	R_s (Ω)
Before RB	3324	4.3
Minimum efficiency (turning point)	2517	7.6
After recovery	3247	5.8

These values show the same trends that were found when the modelling was done for the equivalent circuits (see Table 6.4).

6.5.2 Impedance measurements
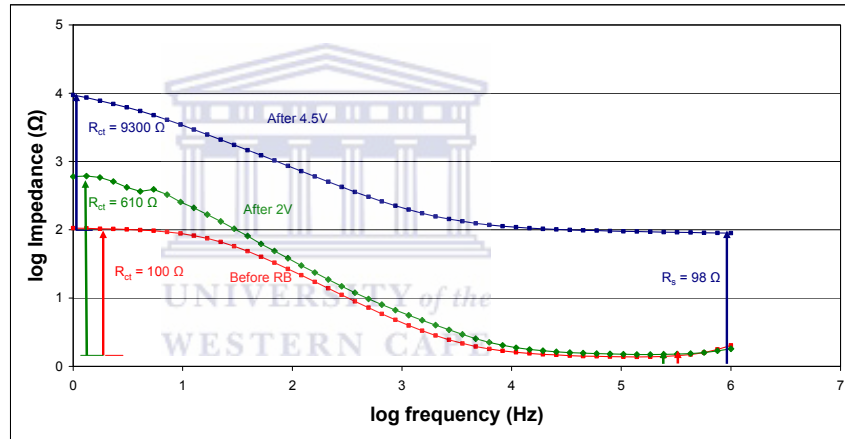
Figure 6.17: Bode plots of the cell before RB (red), after 2 V RB (green) and after 4.5 V RB (blue).

Note the change in the series resistance (R_s), indicated on the right hand side of the graph (Figure 6.17), before RB from 1.4 Ω to 98 Ω after 4.5 V RB. After the cell was subjected to 2 V reverse bias, the charge transfer resistance (R_{ct}) increased to 610 Ω. The value of R_{ct} increased from 100 Ω to 9 300 Ω after the cell was subjected to 4.5 V RB. The positions on the graph which indicates the log(f) of the R_s and R_{ct} were moved apart for clarity. The red, green and blue arrows should be at the same point on the x-axis.
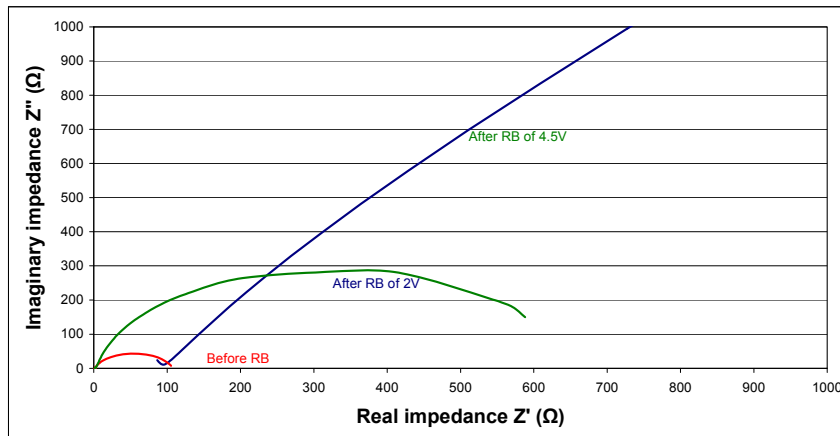
Figure 6.18: Nyquist plots of the cell before RB (red), after 2 V RB (green) and after 4.5 V RB (blue).

The increase in impedance shown in Figure 6.18 also correlates with the trends of increase in resistance that is depicted in the Bode plots (Figure 6.17). The following Figures (6.19 and 6.20) show the Nyquist plots as well as the equivalent circuits of the cells before and after reverse bias.
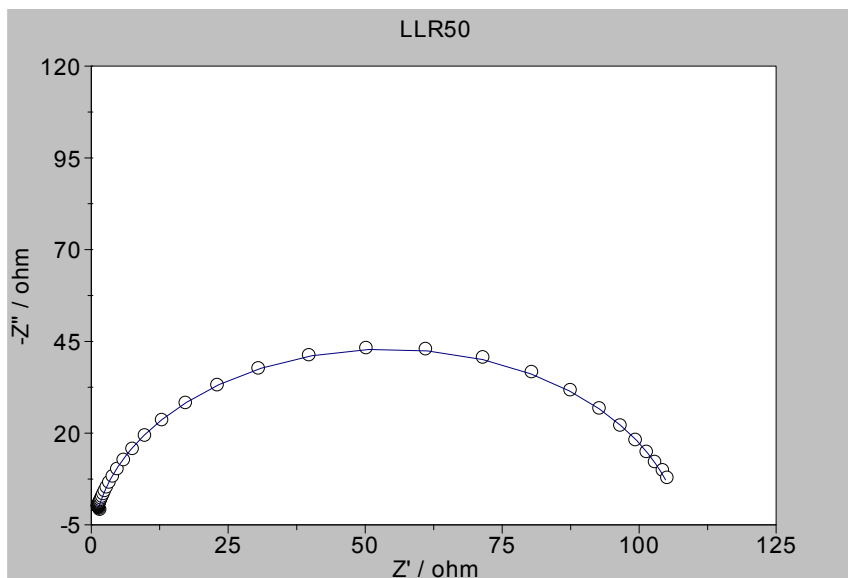
Figure 6.19a: Nyquist plot of a cell before RB
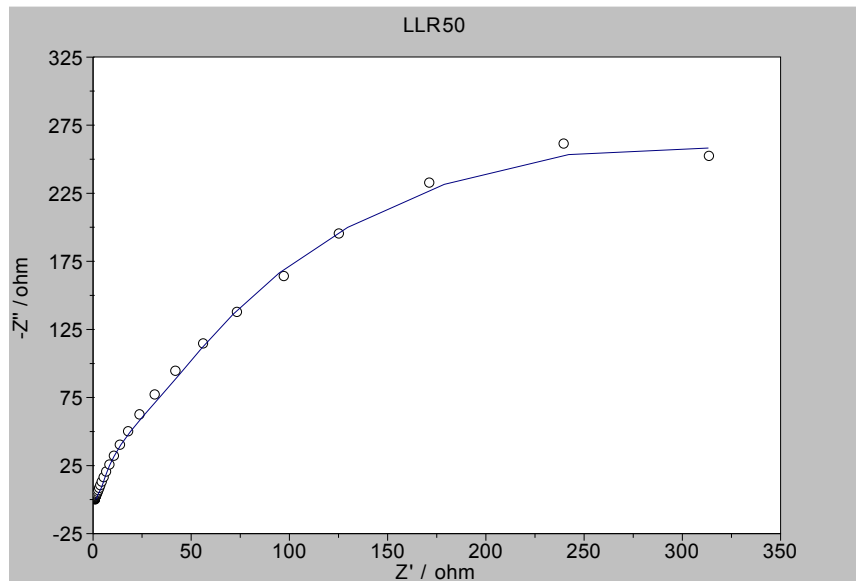
Figure 6.20: Nyquist plot of a cell after RB of 2V
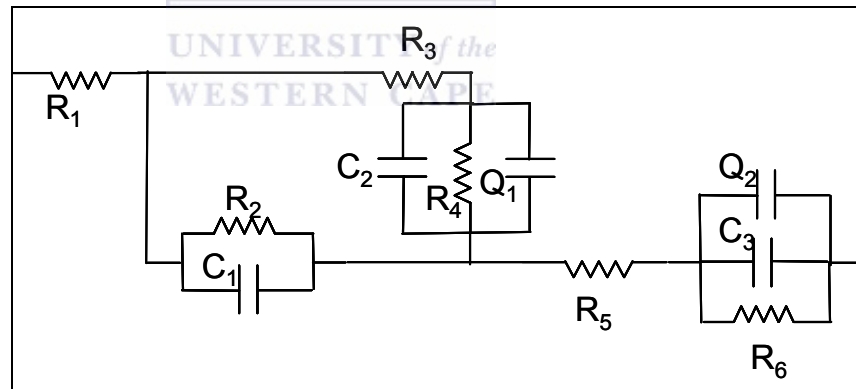
Figure 6.19b: Equivalent circuit of a cell before RB

The equivalent circuit for Figure 6.19a and 6.20 are the same as shown in Figure 6.19b. In all cases the circuits give a good fit as shown in the Nyquist plots. The calculated values of the components before and after reverse bias that are derived from these models are compared in Table 6.4.

The part of the circuit that is shown as R_2, represents the charge transfer resistance for electron recombination at the TiO_2/ITO interface in the cell while C_1 represents the capacitance at the triple contact ITO/TiO_2/electrolyte.

C_2/R_4/Q_1 represents the charge-transfer resistance (R_4) due to the recombination of electrons at the TiO_2/electrolyte interface, the chemical capacitance (C_2) and constant phase element (Q_1) due to a change in electron density. The first indication that a constant phase element exists is that the centre of the semi circle in the Nyquist plot has shifted to below the x-axis. This is evident in both Figures 6.19a and 6.20.

Table 6.4: Numerical values (based on the model of the Nyquist plot) of the different components of the cells before and after RB

	Before RB	After RB of 2 V	After RB of 4.5 V
R_1	0.473 Ω	0.473 Ω	0.459 Ω
C_1	1.00 pF	1.00 pF	0.99 nF
R_2	12.8 mΩ	15.4 mΩ	68.3 Ω
R_3	0.473 Ω	0.473 Ω	0.466 Ω
C_2	22.8 µF	1.00 pF	5.26 µF
R_4	46.8 Ω	146 Ω	8920 Ω
Q_1	4.40×10^{-4}	7.98×10^{-4}	6.56×10^{-4}
n_1	0.833	0.827	0.623
R_5	0.473 Ω	0.473 Ω	23.1 Ω
C_3	10.6 µF	1.00 pF	1.00 pF
Q_2	4.46×10^{-4}	7.97×10^{-4}	1.99×10^{-4}
n_2	0.834	0.829	0.678
R_6	61.3 Ω	208 Ω	8610 Ω

R_3 and R_5 represent the electron transport resistance in the TiO_2 layer. $C_3/Q_2/R_6$ represents the capacitance and charge transfer resistance as well as the constant phase element at the electrolyte/platinum interface in the cell.

R_1, R_3 and R_5 are the series resistance components of the cell and showed no change before or after RB of 2V. The major differences appear to be with the charge transfer resistance (R_2, R_4 and R_6) that indicates that physical changes took place inside the cell as well as at the counter electrode.

The charge transfer resistance at the electrolyte/platinum interface increased from 61 Ω to 208 Ω. Work that was done by Milkevitch *et al.* (1996) indicated that the platinum catalyst can be irreversibly oxidised at voltages of 1.72 V and 1.61 V. The value of the constant phase elements Q_1 and Q_2 doubled while the value of n only increased slightly from 0.827 to 0.833 which relates to 0.5° change in the phase. The capacitance inside the cell (C_2 and C_3) has decreased significantly while the capacitance at the working electrode stayed constant.
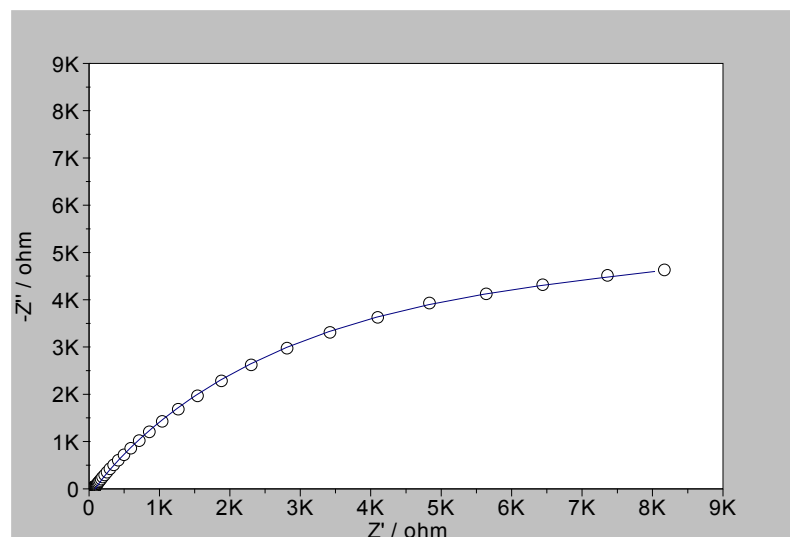
Figure 6.21: Nyquist plot of a cell after RB of 4.5 V

The equivalent circuit of the cell after 4.5 V reverse bias is not different from that of the cell before and after 2 V reverse bias treatment. The series resistance has increased from less than 0.5 Ω to more than 41 Ω. The charge transfer resistance (R_2, R_4 and R_6) increased from a maximum of 108.1 Ω to a maximum of 17.6 kΩ. This cell was irreversibly damaged and no further analysis was carried out.

6.5.3 Cyclic voltammetry

Figure 6.22 shows a kink in the oxidation scan at 0.33 V. After the cell was subjected to reverse bias, this feature did not appear in subsequent scans and was not restored by scanning to negative potentials. The capacitance of the cells decreased after being subjected to reverse bias. This is an indication of irreversible damage due to the oxidation of either the N-C-S groups on the dye or the Pt catalyst on the counter electrode.
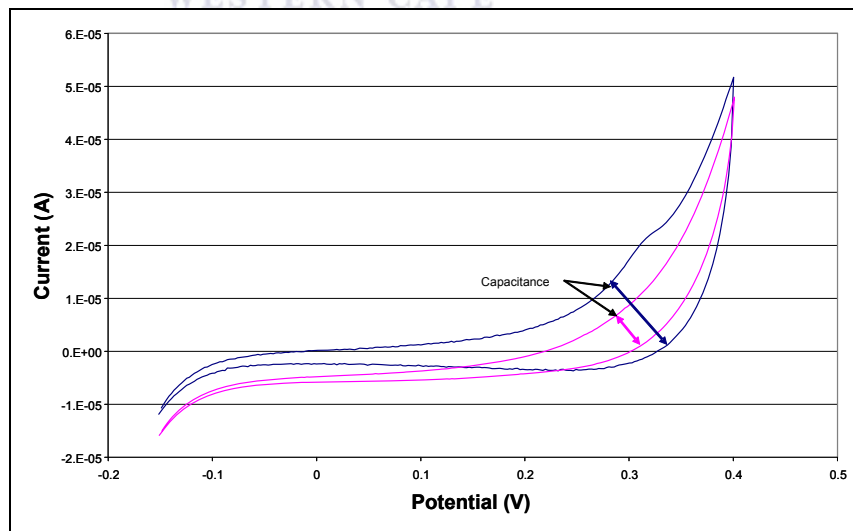
Figure 6.22: Cyclic voltammograms of a cell before and after RB measured in the dark. Note the decrease in the capacitance (narrower) of the pink curve.

6.5.4 Laser beam induced current

The spatially induced current measured across this cell was fairly uniform, typically around 9 μA (see Figure 6.23). The interesting feature on the current map is the increase of current towards the right (red colour). This might have been caused by accumulation of dye sensitive particles to the region during processing of the cell. The small blue region at the bottom centre of the scan corresponds to a visible defect on the cell.
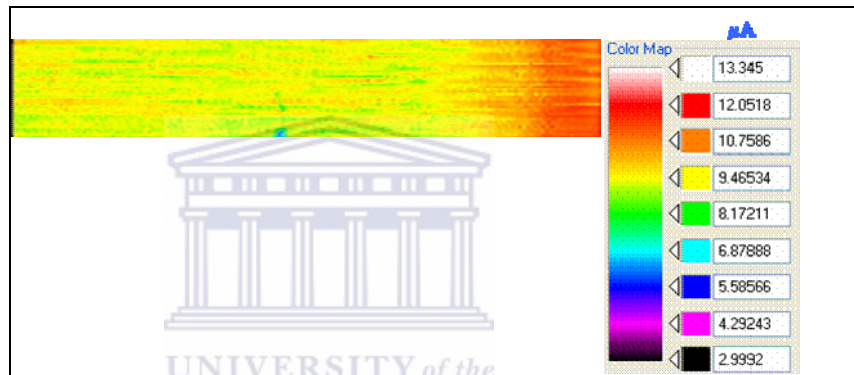
Figure 6.23: An example of the results of an LBIC scan of the surface of a cell. Note the blue spot at the bottom of the cell.
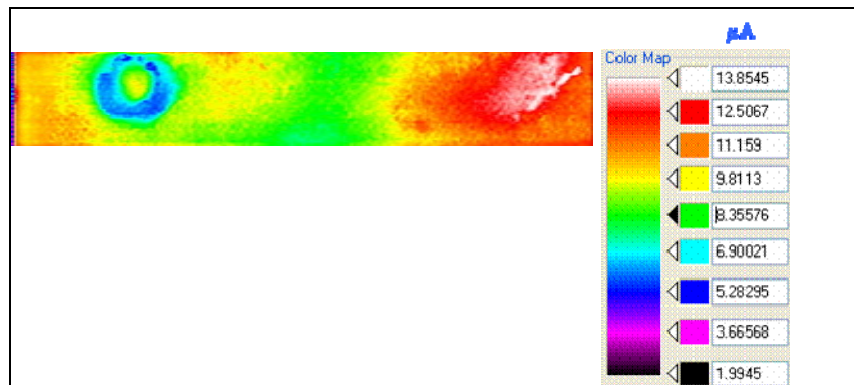
Figure 6.24: An example of the results of an LBIC scan of the surface of a cell. The blue circle is indicative of a defect that was generated in the processing stage of the cell.

The cell was characterised by non-uniformity in induced current. The striking feature in the LBIC map in Figure 6.24 is the ring corresponding to about 5 μA. This again points to non-uniformities that occurred during processing of the cell. Highest currents are generated towards the left edge of the LBIC map. Most of the defects revealed by these LBIC maps maybe minimised during cell processing. Cells with defects were discarded and were not used to obtain any experimental data.

6.5.5 UV-vis
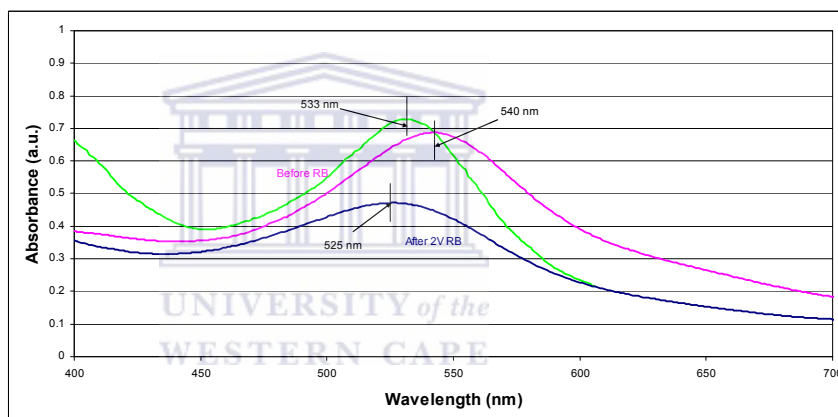
Figure 6.25: UV-vis results of a cell before and after RB. Note the peak shift from 540 to 525 nm. The green graph shows the absorbance of the free dye before adsorbing it on the TiO_2.

When a reverse bias potential of 2 V was applied to the cell the absorption band at 540 nm shifted to 525 nm with a reduction in absorptivity. This absorption band is due to the metal-to-ligand charge transfer (MLCT) from the Ru metal centre to π* orbitals on the pyridyl ligand. The molecule is stabilised by the delocalising effect of the electron donating N-C-S groups. The band shifted to higher energy (blue shift) which resulted in lower cell efficiency.

The absorbance decreased from 0.68 to 0.47 (30%). The decrease in cell efficiency was 42% (from 5.1% to 2.9%) which suggests that this is not the only parameter that changed during the reverse bias.

It was previously determined by Murakoshi *et al*., (1995) that the absorption shifts to lower energies when the complexes are attached to the semiconductor surface. The band shifts were ascribed to the interaction between the dye molecule and the TiO_2 surface through the carboxylic groups. The green graph in Figure 6.25 shows the absorbance band at 533 nm and it shifts to 540 nm after adsorption on the TiO_2 layer. This leads to the possible conclusion that some of the dye was desorbed from the TiO_2 during the reverse bias experiments.

The blue shift could therefore be a combination of the breaking of bonds between the dye and the TiO_2 and the depletion of the N-C-S groups. It was confirmed by FT-IR and Raman that there is no evidence of bond breaking between the TiO_2 and the dye therefore the shift has to be due to the depletion of the N-C-S groups.

6.5.6 Raman measurements

The absence of the characteristic C=O stretch band at 1713 cm^{-1} is an indication that there are no free C=O groups in the cell. This proves that the dye is not desorbed from the titanium dioxide surface. FT-IR spectroscopy measurements also indicated that no desorption of the dye from the TiO_2 film occurred. The peaks at 1540, 1472 and 1610 cm^{-1} represents the bipyridyl groups on the dye molecule (Greijer *et al.,* 2001).
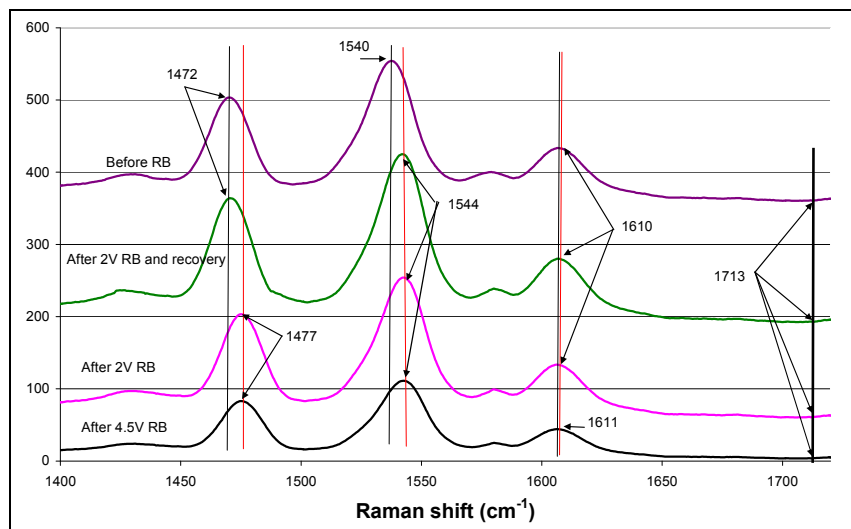
Figure 6.26: Raman spectra of a cell that was subjected to a reverse bias voltage of 2 V and 4.5 V. Note the peak shifts in the original spectrum before reverse bias, after 2 V reverse bias (before and after recovery) and the effect of a reverse bias voltage of 4.5 V. Note the absence of peaks at 1713 cm^{-1}.

During the application of reverse bias potentials, the peaks at 1540 and 1472 cm^{-1} shifted by 5 and 4 cm^{-1} respectively to higher energy while the energy of the band at 1610 cm^{-1} was essentially unchanged. After reverse bias and recovery (2 V), the 1472 cm^{-1} band returned to the original value but the peak initially at 1540 cm^{-1} remained displaced by 4 cm^{-1} to higher energy. The irreversible change to the band at 1540 cm^{-1} suggests that the adsorbed dye has undergone a change directly associated with the bipyridyl ligand. When the cell was subjected to a reverse bias voltage of 4.5 V, neither of the two shifted peaks returned to the original wavenumbers.

6.5.7 FT-IR measurements

The FT-IR measurements were done on a Perkin Elmer Spectra 100 FT-IR spectrometer equipped with Spotlight 400 Imaging System.
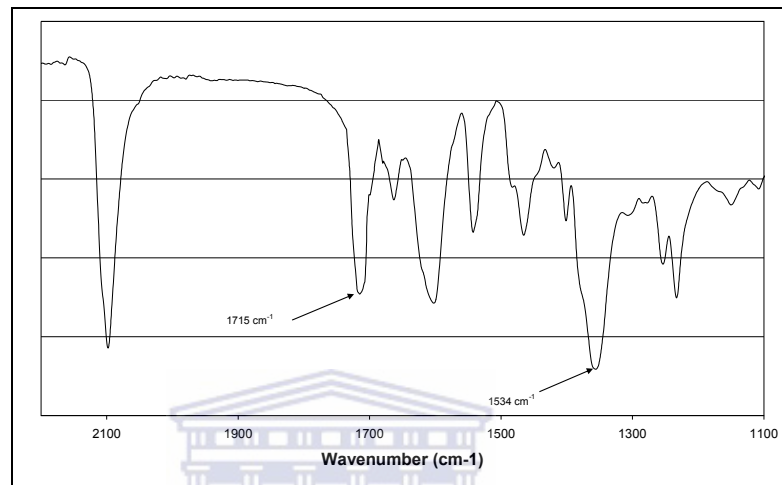
Figure 6.27: FT-IR spectrum of the dye before bonding to the TiO_2 film. Note the marked peaks due to the "free carbonyl groups.
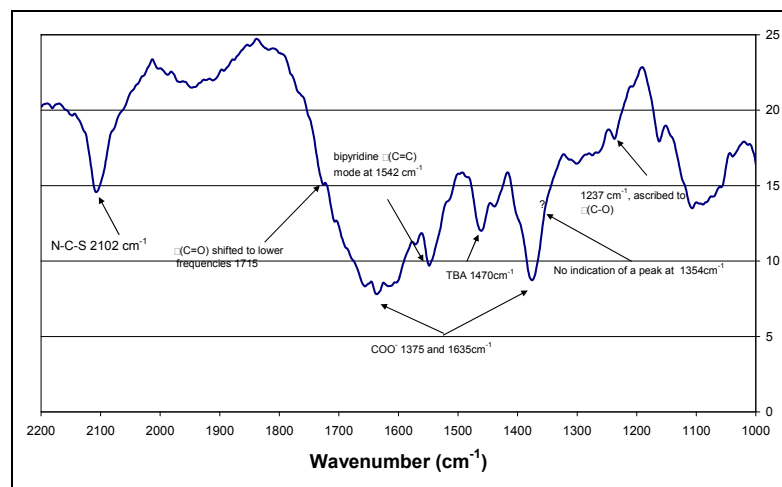
Figure 6.28: FT-IR spectrum of the dye after being subjected to a reverse bias voltage of 2 V.

No evidence could be found of any desorption of the dye carbonyl group from the TiO_2. If there were any isolated (not bound to TiO_2) carbonyl groups, vibrational bands at wavenumbers 1354 cm^{-1} and 1715 cm^{-1} should become evident. This however, was not the case. The strong bands at 1375 cm^{-1} and 1635 cm^{-1} indicated bonded carbonyl groups. Therefore from the FT-IR spectral data it can be stated that there is no disengagement of the dye from the TiO_2 (Figure 6.28). This is also confirmed by results that were obtained by Kuang *et al*., 2006.
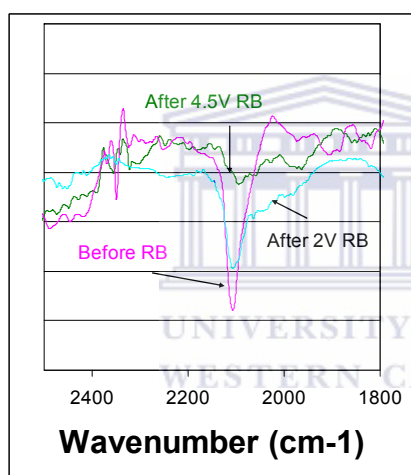
Figure 6.29: The FT-IR spectrum of three cells that were subjected to reverse bias voltages of 2 V and 4.5 V. Note the disappearance of the CN peak at 2100 cm^{-1}.

The spectra in Figure 6.29 shows the effect of the 2 V reverse bias on the N-C-S group in the dye. The N-C-S stretching band was slowly depleted. It seemed as if thiocyanate ion ligand is sensitive to the oxidising effect of the reverse bias on the N-C-S groups. It was suggested by Greijer *et al*., (2001) that a compound analogue to the I_3^- forms:

$$I_2 + SCN^- \longrightarrow I_2SCN^-$$
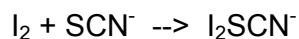
This strongly correlates with the decrease in intensity and blue shift in the UV–vis absorption bands and is attributed to the destabilising effect of the depleting N-C-S group. When the voltage was increased to 4.5 V, the N-C-S vibration band almost disappeared.

6.5.8 SEM measurements

SEM micrographs were obtained before and after the reverse bias potential of 2 V as shown in Figure 6.30 and 6.31. No obvious changes or differences could be detected. This confirms that the morphology did not change due to the reverse bias.
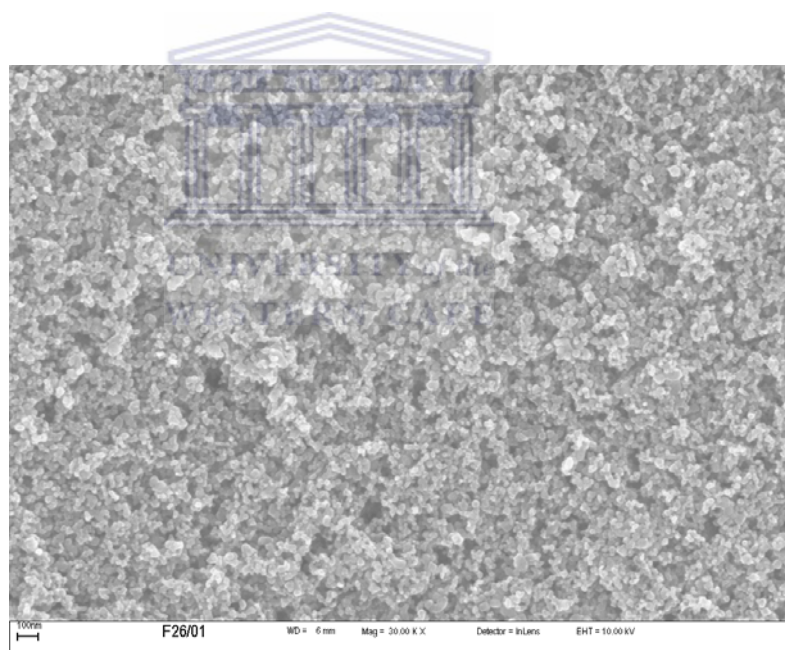
Figure 6.30: SEM micrograph of the TiO_2/dye of a cell before reverse bias.
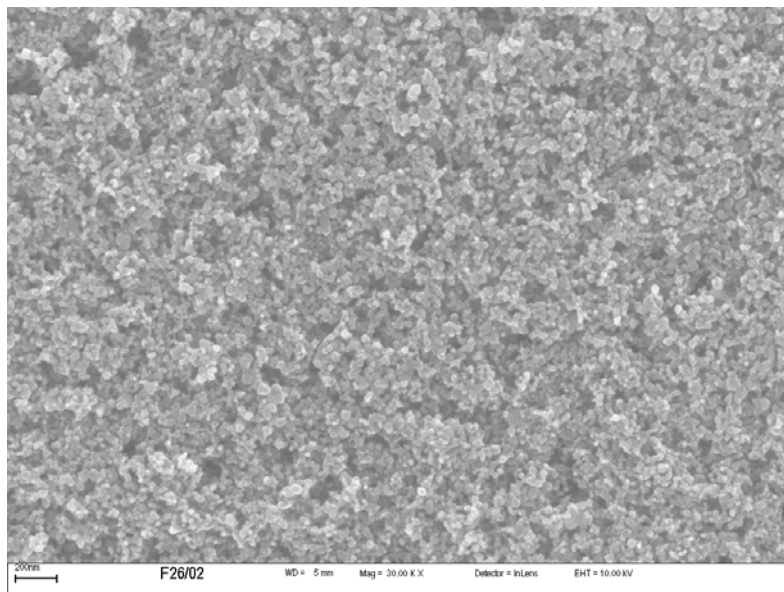
Figure 6.31: SEM micrograph of a cell after it was subjected to a reverse bias potential of 2 V for 500 min.

CHAPTER 7

7   CONCLUSIONS

Nano TiO_2 particles were successfully produced and formulated into a (water base) paste that does not crack when aged. Particles with an average diameter of 25 nm were mixed with particles with an average size of 6 nm in a 1:10 ratio.

We have shown that a reverse bias potential of 2 V resulted in a 42% loss in cell efficiency while 4.5 V caused irreversible damage to a cell and complete loss of performance.

Raman spectroscopy showed the partial recovery of the cell at 2 V reverse bias. The appearance of a vibration band at 1713 cm^{-1} would be evidence of the breaking of the chemisorbed bonds between the dye and the TiO_2 film (dislocation of the dye and the TiO_2). This was not the case and it was also backed up by FT-IR measurements showed no peaks at 1715 cm^{-1} and 1354 cm^{-1} which is characteristic of free carbonyl bonds.

FT-IR however did show the depletion of the N-C-S vibration band at 2100 cm^{-1}.

This work has shown that Raman and FT-IR spectroscopy are complementary techniques that provided structural information of the dye and dye/semiconductor system.

Potentiometric measurements show a significant increase in the charge transfer resistance at the counter electrode which indicates a decrease in the catalytic activity of the Pt. This backs the theory that there is partial oxidation of the Pt that acts as a catalyst for the

regeneration of the Iodide. It was shown by FT-IR that the change was in the dye and not the TiO_2/dye bond.

The values of R_s and R_{sh} that were obtained from the IV curves of the cell under reverse bias showed the same trends that were obtained from the Nyquist plots, Bode plots and equivalent circuits.

It can therefore be stated with confidence that the changes in the cell after being subjected to a reverse bias potential of 2 V for 500 min are attributed to changes on the N-C-S groups on the Ru dye as well as the Pt on the counter electrode.

The morphology of the TiO_2 film on the glass substrate does not change when a cell is subjected to a reverse bias potential of 2 V.

Further research would include different designs of modules that could incorporate the results of this thesis to minimise the effects of reverse bias. A design that would prevent the possibility of a reverse bias voltage of more the one volt should be possible. The design may still have to use diodes but the possibility to use fewer diodes exists.

CHAPTER 8

8 THE NOVELTY AND OUTCOMES OF THIS RESEARCH

8.1 Novelty

The work that is published in this thesis is novel in the following instances:

Cells that were subjected to reverse bias potentials were characterised to determine the changes that took place inside the cell. While I acknowledge that al these techniques have been used individually in characterising DSCs, nobody has used a combination of all these techniques to determine the areas of degradation in a DSC. The combination of optical character (UV-vis), structural nature (Raman, FT-IR and XRD), surface morphology (SEM and LBIC), electrical measurement (I/V curves) and potentiometric measurements (impedance and cyclic voltammetry) were used to show how they compliment each other and confirm or eliminate some of the theories.

Bode plots and Nyquist plots were used as complimentary analysis techniques to determine the changes in charge transfer resistance in the different interfaces in a cell.

Raman spectroscopy was used to determine whether there was any dislocation of the dye and TiO_2.

FT-IR spectroscopy was used to determine whether there were any structural changes to the dye and to confirm results from the Raman spectra regarding the bond between the dye and the TiO_2.

8.2   Papers/posters that were presented on this work.

1. *Dye Solar Cells. (Artificial photosynthesis).*
Le Roux, L.J., Hietkamp, S., Knoesen, D. and Arendse, C. A poster was presented at the 51st Annual Conference of the SAIP at UWC, July 2006.

2. *Dye solar cells (and PVs) in South Africa.*
Le Roux, L.J. A paper presented at the Industrialisation of DSC from research to Product, Canberra, Australia, February 2006.

3. *The chemical stability of Dye Solar Cells under Reverse Bias.*
Le Roux, L.J. A poster was presented at the NanoEurope Conference in St Gallen, Switzerland, August 2007.

4. *Electron Migration and Stability of Dye Solar Cells*.
Le Roux, L.J. and Hietkamp, S. A paper was presented at the 1st International Symposium on Electrochemistry in South Africa, July 2008.

5. *Dye Solar Cell Research in South Africa.*
Le Roux, L.J. A paper was presented at the IBSA (India, Brazil, and South Africa) workshop at Pilanesberg, June 2008.

6. *Dye solar cells: A different approach to solar energy.*
Le Roux L.J., Hietkamp, S. and Cummings, F.R. A paper was presented at the CSIR Outcomes Conference, November 2008 and published in the Proceedings of the 2nd CSIR Biennial Conference - Science real and relevant.

7. *Spectroscopic and Impedance Studies of Reverse Biased Degraded Dye Solar Cells.*

L.J. le Roux, D. Knoesen and S. Hietkamp. This paper was submitted for publication in *Journal of Solid State Electrochemistry* and is currently under review.

REFERENCES

Aarik, J., A., Kiisler, A., Uustare, T. and Sammelselg, V., 1997. Effect of crystal structure on optical properties of TiO_2 films grown by atomic layer deposition. *Thin Solid Films,* 305, Issues 1-2, p.270-273.

American Society for Testing and Materials (ASTM) Terrestrial Reference Spectra for Photovoltaic Performance Evaluation: http://rredc.nrel.gov/solar/ spectra/am1.5, 2005.

Agrell, H.G., Lindgren, J. and Anders Hagfeldt, A., 2003. Degradation mechanisms in a dye-sensitized solar cell studied by UV–VIS and IR spectroscopy. *Solar Energy.* 75(2), p.169-180.

Bach U., Tachibana Y., Moser J. E, Haque S.A., Durrant J.R., Grätzel M. and Klug D.R., 1999. Charge Separation in Solid-State Dye-Sensitized Heterojunction Solar Cells Laboratory. *J. Am. Chem. Soc.,* 121, p.7445-7446.

Bard, A. J. & Faulkner, L. R., 1980. Electrochemical Methods. New York: John Wiley and Sons.

Bauer, C., Boschloo, G., Mukhtar, E., and Hagfeldt, A., 2002. Interfacial Electron-Transfer Dynamics in Ru(tcterpy)(NCS)3-Sensitized TiO_2 Nanocrystalline Solar Cells. *J. Phys. Chem. B.,* 106, p.12693.

Bauer, C., Boschloo, G., Mukhtar, E. and Hagfeldt, A., 2002. Ultrafast studies of electron injection in Ru dye sensitized SnO_2 nanocrystalline thin film. *International Journal of Photoenergy,* 4, p.17-20.

Bay, L. & West, K., 2005. An equivalent circuit approach to the modelling of the dynamics of dye sensitized solar cells *Solar Energy Materials & Solar Cells,* 87, p.613–628.

Bisquert, J., Cahen, D., Hodes, G., Ruhle, S., and Zaban, A., 2004. Physical Chemical Principles of Photovoltaic Conversion with

Nanoparticulate, Mesoporous Dye-Sensitized Solar Cells. *J. Phys. Chem. B.,* 108, p.8106-8118.

Bisquert, J., 2004. Impedance Spectroscopy applied on solar cells. *Nordic Workshop on Solar Electricity. Sonnerupgaard Gods*, Denmark, p.27-29.

Cahen, D., Hodes, G., Grätzel, M., Guillemoles, J.F. and Riess, I., 2000. Nature of Photovoltaic Action in Dye-Sensitized Solar Cells. *J. Phys. Chem. B., 104, p.*2053-2059.

Dloczik, L., Ileperuma, O., Lauermann, I., Peter, L.M., Ponomarev, E.A.,Redmond, G., Shaw, N.J. and Uhlendorf, I., 1997. Dynamic Response of Dye-Sensitized Nanocrystalline Solar Cells: Characterization by Intensity-Modulated Photocurrent Spectroscopy. *J. Phys. Chem. B*., 101, p.10281-10289.

Fabregat-Santiago, F., Bisquert, J., Garcia-Belmonte, G., Boschloo, G. and Hagfeldt, A., 2003. Cyclic Voltammetry Studies of Nanoporous Semiconductors. Capacitive and Reactive Properties of Nanocrystalline TiO_2 Electrodes in Aqueous Electrolyte. *J. Phys. Chem. B, 107,* p.758-768.

Fabregat-Santiago, F., Bisquert, J., Garcia-Belmonte, G., Boschloo, G. and Hagfeldt, A., 2005. Influence of electrolyte in transport and recombination in dye-sensitized solar cells studied by impedance spectroscopy. *Solar Energy Materials and Solar Cells*, 87, p.117-131.

Falaras, P., 1998. Synergetic effect of carboxylic acid functional groups and fractal surface characteristics for efficient dye sensitization of titanium oxide. *Solar Energy Materials and Solar Cells.* 53, p.163-175.

Falaras, P., Gratzel, M., Hugof LeGoff, A., Nazeeruddin, M.K. and Vrachnou, E., 1993. Dye sensitization of TiO_2 surfaces studied by Raman spectroscopy, *J. Electrochem. Soc.* 140, L92–L94.

Fischer, A.C., Peter, L.M., Ponomarev, E.A., Walker, A.B. and Wijayantha, K.G.U., 2000. Intensity Dependence of the Back

Reaction and Transport of Electrons in Dye-Sensitized Nanocrystalline TiO$_2$ Solar Cells. *J. Phys. Chem. B.,* 104*,* p.949-958.

Finnie, K.S., Bartlett, J.R. and Woolfrey, J.L., 1998. Vibrational Spectroscopic Study of the Coordination of (2,2¢-Bipyridyl-4,4¢-dicarboxylic acid)ruthenium(II) Complexes to the Surface of Nanocrystalline Titania. *Langmuir*, 14, p.2744-2749.

Gao, K. and Wang, D., 2007. Raman study of photo-induced degradation of the Ru(II) complex adsorbed on nanocrystalline TiO$_2$ films. *Physica Status Solid.Rapid Research letters.* 1(2), p.R83-R58.

Grätzel M., 2001. Photoelectrochemical cells. *Nature*, 414.

Grätzel M., 2006. Photovoltaic performance and long-term stability of dye-sensitized meosocopic solar cells. *Comptes Rendus Chimie,* 9.

Grätzel, M. and McEvoy, A.J., 2004. Hydrogen Production by Solar Photolysis of Water. *American Physical Society Symposium* Montreal, Canada.

Gxasheka, A.R., van Dyk, E.E. and FJ Vorster, F.J., 2005. Characterization of photovoltaic devices by means of laser beam-induced current scanning: its value as a diagnostics tool. *S.A. J. Sci*. 101, p. 285-287.

Hagfeldt, A and Grätzel, M., 1995. Light-induced redox reactions in nanocrystalline systems. *Chem. Rev*. 95, p.49-68.

Hagfeldt, A., Lindquist, S. E., Grätzel, M., 1994. *Solar Energy Materials and Solar Cells,* 32, p.245.

Halme, J., Toivola, M., Tolvanen, A. and Lund, P., 2006. Charge transfer resistance of spray deposited and compressed counter electrodes for dye-sensitized nanoparticle solar cells on plastic substrates. *Solar Energy Materials and Solar Cells*, 90 (7-8), p. 872-886.

Han, L., Koide, N., Chiba, Y., Islam, A., and Mitate, T., 2006. Modelling of an equivalent circuit for dye-sensitized solar cells:

improvement of efficiency of dye-sensitized solar cells by reducing internal resistance. *Comptes Rendus Chimie,* 9*,* p.645–651.

Haque, S.A., Tachibana, Y., Klug, D.R. and Durrant, J.R., 1998. Charge Recombination Kinetics in Dye-Sensitized Nanocrystalline Titanium Dioxide Films under Externally Applied Bias. *J. Phys. Chem. B.,* 102, p.1745-1749.

Haque, S.A., Tachibana, Y., Willis, R.L., Moser, J.E., Grätzel, M., David, R., Klug, D.R., James, R. and Durrant J.R., 2000. Parameters Influencing Charge Recombination Kinetics in Dye-Sensitized Nanocrystalline Titanium Dioxide Films. *J. Phys. Chem. B.,* 104, p.538-547.

Hedbor, S and Klar, L., 2005. Plant Extract Sensitised Nanoporous Titanium Dioxide Thin Film Photoelectrochemical Cells Copyright©Sigrid Hedbor and Department of Engineering Sciences, *Solid State Physics*, Uppsala University. UPTEC W 05-016, ISSN 1401-5765.

Hinsch, A., Belledin, U., Brandt, H., Einsele, F., Hemming, S., Koch, D., Rau, U., Sastrawan, R., and Schauer, T., 2006. Glass Frit Sealed Dye Solar Modules With Adaptable Screen Printed Design. Paper presented at the 4th *World Conference on Photovoltaic Energy Conversion*: Hawaii.

Hoshikawa, T., Ikebe, T., Kikuchi, R. and Eguchi, K., 2006. Effects of electrolyte in dye-sensitized solar cells and evaluation by impedance spectroscopy. *Electrochimica Acta,* 51, Issue (25), p,5286-5294.

http://www.physclips.unsw.edu.au/jw/AC.html (2006).

http://www.solaronix.com/technology/dyesolarcells (2006).

http://www.swarthmore.edu/NatSci/echeeve1/Ref/LPSA/Bode/Bode.html (2006).

Huang, S.Y., Schlichthörl, G., Nozik, A.J., Grätzel, M. and Frank, A.J., 1997. Charge Recombination in Dye-Sensitized Nanocrystalline TiO_2 Solar Cells. *J. Phys. Chem. B.,* 101, p.2576-2582.

Johanssen, E., 2006. Interfaces in Dye-Sensitized Oxide / Hole-Conductor Heterojunctions for Solar Cell Applications. *Digital Comprehensive Summaries of Uppsala. Dissertations from the Faculty of Science and Technology,* 188.

Kalyanasundaram, K. & Grätzel, M., 1998. Applications of Functionalized Transition Metal Complexes in Photonic and Optoelectronic devices. *Coord. Chem. Rev.*, 77, p.347-414.

Kalyanasundaram, K. and Grätzel, M., 1994. Artificial photosynthesis: Efficient dye-sensitized photoelectrochemical cells for the direct conversion of sunlight to electricity. *Curr. Science,* 66, p.706-715.

Karden, E., Buller, S. and De Doncker, R. W., 2000. A method for measurement and interpretation of impedance spectra for industrial batteries. *Journal of Power Sources,* 85, 72-78.

Kaiser optical systems, inc. http://www.kosi.com/raman/resources (2005).

Kern, R., Ferber, J., Hinsch, A., Kroon, J., Luther, J., Meyer, A., Sastrawan, R., Uhlendorf, I., 2001. Investigation of the long-term stability of dye-sensitized solar cells by optical and electrochemical impedance spectroscopy. *Proceedings of the 13th Workshop on Quantum Solar Energy Conversion - (QUANTSOL).*

Kern, R., Sastrawan, R., Ferber, J., Stangl, R., Luther, J., 2002. Modelling and interpretation of electrical impedance spectra of dye solar cells operated under open-circuit conditions. *Electrochimica Acta* 47, p.4213-4225.

Kohle, O., Grätzel, M., Meyer, A.F. and Meyer, T.B., 1997. The photovoltaic stability of bis(isothiocyanato)ruthenium(II)-bis-2,2'-bipyridine-4,4'-dicarboxylic acid and related sensitizers. *Advanced Materials,* 9(11), p.904.

Kuang, D., Ito, S., Wenger, B., Klein, C., Moser, J., Humphry-Baker, R., Zakeeruddin, S.M. Grätzel, M., 2006. High Molar Extinction

Coefficient Heteroleptic Ruthenium Complexes for Thin Film Dye-Sensitized Solar Cells. *J. Am. Chem. Soc.,* 128 (12), p.4146-4154.

Leggat, R. A., 1999. History of Photography. http://www.rleggat.com/photohistory/history/vogel.htm, (2006).

Markvart, T. and Castañer, L., 2003. Practical Handbook of Photovoltaics: Fundamentals and Applications. New York. Elsevier, p.81 – 87.

Martin J., Femandez-Lorenzo C., Alcantara R., Poce-Fatou J. A., Anta J. A., Casanueva F., Oskam G. and Gombert A., 2006. Application of correction algorithms for obtaining high-resolution LBIC maps of dye-sensitized solar cells. *Society of Photo-Optical Instrumentation Engineers, Bellingham, WA, ETATS-UNIS.*

Menzies, D.B., Dai, Q., Bourgeois, L., Caruso, R.A., Cheng, Y., Simon, G.P. and Spiccia, L., 2007. Modification of mesoporous TiO_2 electrodes by surface treatment with titanium(IV), indium(III) and zirconium(IV) oxide precursors: preparation, characterization and photovoltaic performance in dye-sensitized nanocrystalline solar cells. *Nanotechnology* ,18, p125608.

Milkevitch, M.; Brauns, E. and Brewer, K.J. (1996). Spectroscopic and Electrochemical Properties of a Series of Mixed-metal d^6,d^8 Bimetallic Complexes of the Form $[(Bpy)_2m(BL)PtCl_2]^{2+}$ (Bpy = 2,2‘-Bipyridine; BL = dpq (2,3-Bis(2- Pyridyl)Quinoxaline) Or dpb (2,3-Bis(2-Pyridyl)- Benzoquinoxaline); M = Os^{ii} Or Ru^{ii}). *Inorganic Chemistry*, 35 (6)*, p.1737-1739.*

Murakoshi,K., Kano, G., Wada, Y., Yanagida, S., Miyazaki, H., Matsumoto, M. and Murasawa, S., 1995. Importance of binding states between photosensitizing molecules and the TiO_2 surface for efficiency in a dye-sensitized solar cell. *Journal of Electroanalytical Chemistry,* 396, p.27-34.

Nazeeruddin, M.K., Kay, A., Rodicio, I., Humpbry-Baker, R., Miiller, E., Liska, P., Vlachopoulos, N. and Grätzel, M., 1993. Conversion of Light to Electricity by cis-XzBis(2,2'-bipyridyl-4,4'-dicarboxylate) ruthenium(ii) Charge-Transfer Sensitizers (X=C1⁻, Br⁻, I⁻, CN⁻, and

SCN$^-$) on Nanocrystalline TiO$_2$ Electrodes *J. Am. Chem. Soc.,* 115, p.6382-6390.

Nusbaumer, H., (2004). Alternative Redox Systems for the Dye-Sensitized Solar Cell. PhD. thesis. École Polytechnique Fédérale De Lausanne (EPFL), Switzerland.

O'Regan, B and Grätzel, M., 1991. A low-cost, high-efficiency solar cell based on dye-sensitized colloidal TiO$_2$ films. *Nature* 353, p.737-740.

Peter, L.M., Wijayantha, K.G.U., 1999. Intensity dependence of the electron diffusion length in dye-sensitised nanocrystalline TiO$_2$ photovoltaic cells. *Electrochemistry Communications,* 1, p.576–580.

Peter L.M., Duffy N.W., Wang R.L. and Wijayantha K.G.U., 2002. Transport and interfacial transfer of electrons in dye-sensitized nanocrystalline solar cells. *Journal of Electroanalytical Chemistry* 524–525, p.127–136.

Pitarch, A.; Garcia-Belmonte, G.; Mora-Sero, I.; Bisquert, J., 2004. Electrochemical impedance spectra for the complete equivalent circuit of diffusion and reaction under steady-state recombination current. *Phys. Chem. Chem. Phys*. 6, p.2983.

Porkodi, K. and Arokiamary, S. D., 2007. Synthesis and spectroscopic characterization of nanostructured anatase titania: A photocatalyst. *Materials Characterization*, 58(6), p.495-503

Sastrawan, R*.,* Renz, J., Prahl, C., Beier, J., Hinsch, A. and Kern, R., (2006). Interconnecting dye solar cells in modules—*I–V* characteristics under reverse bias. *Journal of Photochemistry and Photobiology A*: Chemistry, 178, p.33–40.

The Nobel Prize internet archive. http://almaz.com/nobel/nobel.html (2006)

Stapleton, J., 2005. http://www.mri.psu.edu/facilities/MCL/techniques/UV-Vis/UV-VisTheory.asp.

Van Zeghbroeck, B. 2004. Principles of semiconductor devices. Available: http://ece-www. colorado.edu/~bart/book/book/title.htm

Wang Q., Moser Jacques-E. and Grätzel M., 2005. Electrochemical Impedance Spectroscopic Analysis of Dye-Sensitized Solar Cells. *J. Phys. Chem. B,* 109, p.14945-14953.

Wheatley M.G., McDonagh A.M., Brungsa M.P., Chaplina R.P. and Sizgekc E., 2003. A study of reverse bias in a dye sensitised photoelectrochemical device. *Solar Energy Materials & Solar Cells* 76, p.175–181.

Würfel, P., (2005). *The Physics of Solar Cells*. Weinheim: Wiley-VCH.

APPENDIX

XRD analysis of the nano TiO_2 that was synthesized in our labopratory.

CERTIFICATE OF ANALYSIS

Analyses:	
Description of samples:	Characterization of Degussa P25 anatase and of LLR34 Final
	TiO₂, including domain size
	Both are white powders
Identification of samples:	HL4032Gc (P25), HL403R3b (LLR34)
Analysed for:	Mr L Le Roux, M&MTEK CSIR
Analysis procedure:	X-ray powder diffraction (XRPD)
Date sample received	14 January 2005
Date sample analysed	21-22 January 2005

1. PROCEDURE

The P25 sample did not require comminution. The LLR34 sample required further slight comminution. The sample was hard. The samples were back pressed into a steel ring and analysed.

The X-ray powder diffraction generator used was a Phillips PW 1830 generator operating at 40 kV and 40 mA. Copper Kα₁ radiation with a wavelength of 1.54060 Å was used. The samples were run from 4° to 140° 2θ, step size 0.02° 2θ and step time 4 seconds. Phase identification was accomplished through comparison of the diffractograms with standard data from the ICDD[1] and calculation of the unit cell lattice constants with a non-linear least squares refinement[2]. The percentage semi-quantitative analyses were calculated using the XPert High Score Plus software which uses the Reference Intensity Ratio (RIR) method[4]. The percentage quantitative analyses were calculated using the X'Pert High Score Plus software[3] which uses the Rietveld refinement method[5]. In this case the automatic Rietveld mode[3] with default parameters and fitted background was used. The size-strain analyses were done in a similar fashion to the example given in the X'Pert High Score Plus manual[3] except that the receiving slit was kept at 0.1 mm and not changed to 0.3 mm. The NBS[6] cerium oxide was used as the instrument standard to determine the instrumental broadening.

Analysed by	(012-841-3373)	Checked by	(012-841-2607)	For Director	
Paul Boucher (Approved Signatory) Metrologist		Retha Rossouw Metrologist		Business Area Manager	
Date of issue 25 February 2005		Page 1 of 11		Certificate number SAM – 685	

2. RESULTS

The XRD diffractograms are attached in Appendix A. In the LLR34 diffractograms the line at 130° is a smoothing error. The crystalline phases identified in the samples are given in Table 1. The content description is based on the relative intensity of the strongest peak of the phase of 100 - 50% major, 49 - 20% minor, 19 - 5% little and <5% trace.

Table 1: Crystalline phases identified in the samples.

Content	P25	LLR34
Major	anatase	anatase
Minor	-	-
Little	rutile	brookite, unidentified
Trace	unidentified	-

The major crystalline phase in the P25 sample is anatase, a little rutile and a trace of an unidentified phase/s. In the peak angle listing of the diffractogram 40 of the 41 peaks were accounted for. The unidentified peak had an intensity of 0.1%. No major amount of amorphous material seems to be present.

The major crystalline phase in the LLR34 sample is anatase and, a little brookite and un-identified phase/s. In the peak angle listing of the diffractogram 7 of the 8 broadened peaks were accounted for. The unidentified peak had an intensity of 10.1%.

3. DISCUSSION

The calculated[2] XRD parameters of the phases identified in the samples are compared with one of their standard patterns[1] and are given in Table 2.

The first column of Table 2 gives the mineralogical name of the phase, followed by its normal chemical composition and finally its crystal system. Columns 3 to 5 give the dimensions of the unit cell axes, a, b and c. The number in brackets following the lattice parameter is the precision standard deviation expressed on the last decimal value. Column 6 gives the fixed interaxial angles, α is the angle between unit axes b and c, β the angle between a and c, and γ the angle between a and b. Columns 7 and 8 give the volume of the unit cell and the percentage change of this volume compared to the quoted standard pattern, respectively. The 9th column gives the ratio of the number of peaks used in the calculation of the identified phase over the total number in the peak angle listing of the diffractogram; note that overlaps occur. The 10th column gives a range of the percentage semi-quantitative mass analyses[4] of the identified phases. This range is obtained by a RIR recalculation after a pattern shift of 4 times the full width at half maximum (FWHM) for each phase. The last column gives the percentage quantitative mass analyses[5] of the identified phases. In the last column the R weighted pattern[5] (Rwp), a crystallographic Rietveld criteria of fit is also given. The smaller the Rwp the better the fit.

Analysed by	(012-841-3373)	Checked by	(012-841-2607)	For Director	
Paul Boucher (Approved Signatory) Metrologist		Retha Rossouw Metrologist		Business Area Manager	
Date of issue 25 February 2005		Page 2 of 11		Certificate number SAM – 685	

Table 2: Comparison of the calculated XRD parameters between the identified phases and their standard patterns.

Phase	Reference	a (Å)	b (Å)	c (Å)	α=β=γ (°)	V (Å³)	ΔV (%)	#lines /total	~Mass (%)*	Mass (%)*
Anatase (TiO₂, tetragonal)	P25 21-1272†	3.785(1)	-	9.509(3)	90	136.25	-0.04	29/41	92,1	Rwp= 15,34
		3.7852		9.5139	90	136.31		39/39		
Rutile (TiO₂, tetragonal)	P25 65-0191†	4.593(1)	-	2.958 (1)	90	62.41	0.00	12/41	7,9	Rwp= 15,34
		4.5933		2.958	90	62.41		43/43		
Not identified	P25	-	-	-	-	-	-	1/41	14-11	
Anatase (TiO₂, tetragonal)	LLR34 71-1168†	3.818(7)	-	9.486(8)	90	138.29	0.13	5/8	87,6	Rwp= 10,92
		3.797(4)		9.579(1)	90	138.11		18/18		15,34
Brookite (TiO₂, orthorhombic)	LLR34 76-1936†	9.237(6)	5.466(1)	5.130(1)	90	259.02	0.03	5/8	12,4	
		9.191(4)	5.463(4)	5.157(4)	90	258.94		90/90		
Not identified	LLR34	-	-	-	-	-	-	1/8	-†	Rwp= 10,92

* Mass content does not take into account the unidentified content.
† Calculation not possible because main peak is overlapped.

The calculated unit cell axes and volumes in Table 2 compare well with the standard parameters. The standard deviations also indicate a good fit of the data to the calculated unit cells. Further investigation of the unidentified peaks in the samples is beyond the scope of this investigation.

The calculated[3] size and strain results are given in Table 3. The number in brackets following the size or strain result is the R weighted pattern[5] (R_{wp}).

Table 3: Size and strain results.

Sample	Size & strain	Size only	Strain only	None
P25 anatase (R_{wp})	226 Å: 0.13 % (12,2)	215 Å (12,3)	0,33 % (18,0)	(12,2)
P25 rutile (R_{wp})	302 Å: 0.00 % (12,2)	373 Å (12,3)	0,10 % (18,0)	(12,2)
LLR34 anatase (R_{wp})	41 Å: 0.31 % (14,6)	40 Å (14,8)	1,17 % (24,2)	(36,8)

The P25 result for size and strain of 22.6 nm compares well with the nominal particle size of 25 nm. In the P25 case, the rutile content varies from 7.6 to 8.0% for the size-strain analyses of anatase and rutile. Table 3 confirms that the LLR34 anatase crystallites (i.e. coherently scattering domains) are smaller (4.1 nm) than the P25 anatase ones (22.6 nm). The P25 and LLR34 strain only results and, the LLR34 no size and no strain results, can be disregarded because of their higher R_{wp} values. In the LLR34 case, size-strain analyses of anatase and brookite were unreliable because the refinement became unstable for unknown reasons at this stage, the brookite content varied from 0 to 30%.

4. CONCLUSIONS

The major crystalline phase in the P25 sample is anatase, a little rutile and a trace of an unidentified phase/s. In the peak angle listing of the diffractogram 40 of the 41 peaks were accounted for. The unidentified peak had an intensity of 0.1%. No major amount of amorphous material seems to be present.

The major crystalline phase in the LLR34 sample is anatase and, a little brookite and un-identified phase/s. In the peak angle listing of the diffractogram 7 of the 8 broadened peaks were accounted for. The unidentified peak did not have an intensity greater than 10,1%.

The P25 result for size and strain of 23 nm compares well with the nominal particle size of 25 nm. It is confirmed that the LLR34 anatase crystallites (i.e. coherently scattering domains) are smaller (4 nm) than the P25 anatase ones (23 nm).

5. REFERENCES

[1] INTERNATIONAL CENTRE FOR DIFFRACTION DATA, "Powder Diffraction File", Pennsylvania, USA, 2003.

[2] RAJABALEE, F A, "Wincell 1.1: A Windows package for DOS routines for unit cell refinements", Bordeaux, France, updated March, 2000.

[3] PANalytical, B.V., "X'Pert HighScore Plus", (PW 3212), Almelo, Holland, March, 2004.

[4] CHUNG, F H, "Quantitative Interpretation of X-Ray Diffraction Patterns of Mixtures. II. Adiabatic Principle of X-Ray Diffraction Analysis of Mixtures". J. Appl. Cryst., 7, 526-531, 1974.

[5] YOUNG, R A (editor), "The Rietveld Method", International Union of Crystallography and Oxford University Press, Oxford, 2002.

[6] NATIONAL BUREAU OF STANDARDS, "Standard Reference Material 674, X-Ray Powder Diffraction Intensity Set", CeO₂, Washington, 1983.

6. REMARKS

6.1 The results in this report relate only to the sample(s) mentioned herein.

6.2 Certain of the NML certificates are consistent with the CSIR-NML capabilities that are included in Appendix C of the MRA (Mutual Recognition Arrangement) drawn up by the CIPM. Under the MRA, all participating institutes recognise the validity of each other's calibration and measurement certificates for the quantities and ranges and measurement uncertainties specified in Appendix C. For details see http://www.bipm.org.

6.3 The analyses were carried out at an ambient temperature of 22°C ± 4°C and a relative humidity of 40% RH ± 10% RH.

6.4 The NML scopes of accreditation can be viewed on the NML Internet site http://www.nml.csir.co.za or the SANAS web site http://www.sanas.co.za.

6.5 The final report will be the property of the client and may be published by him, provided that it is published in full, or where only extracts therefrom or a summary or an abridgement thereof is published, the CSIR's prior written approval of the extracts, summary or abridged report be obtained.

Analysed by	(012-841-3373)	Checked by	(012-841-2607)	For Director	
Paul Boucher (Approved Signatory)		Retha Rossouw		Business Area Manager	
Metrologist		Metrologist			
Date of issue		Page 5 of 11		Certificate number	
25 February 2005				SAM – 685	